

Metal-poor star formation triggered by the feedback effects from Pop III stars

Gen Chiaki,^{1*} Hajime Susa¹ and Shingo Hirano²

¹*Department of Physics, Konan University, 8-9-1 Okamoto, Kobe, 658-0072, Japan*

²*Department of Astronomy, The University of Texas at Austin, Austin, TX 78712, USA*

ABSTRACT

Metal enrichment by the first-generation (Pop III) stars is the very first step of the matter cycle in the structure formation and it is followed by the formation of extremely metal-poor (EMP) stars. To investigate the enrichment process by the Pop III stars, we carry out a series of numerical simulations including the feedback effects of photoionization and supernovae (SNe) of Pop III stars with a range of masses of minihaloes (MHs), M_{halo} , and Pop III stars, M_{PopIII} . We find that the metal-rich ejecta reaches neighbouring haloes and external enrichment (EE) occurs when the halo binding energy is sufficiently below the SN explosion energy, E_{SN} . The neighbouring haloes are only superficially enriched, and the metallicity of the clouds is $[\text{Fe}/\text{H}] < -5$. Otherwise, the SN ejecta falls back and recollapses to form enriched cloud, i.e. internal enrichment (IE) process takes place. In case that a Pop III star explodes as a core-collapse SNe (CCSNe), MHs undergo IE, and the metallicity in the recollapsing region is $-5 \lesssim [\text{Fe}/\text{H}] \lesssim -3$ in most cases. We conclude that IE from a single CCSN can explain the formation of EMP stars. For pair-instability SNe (PISNe), EE takes place for all relevant mass range of MHs, consistent with no observational sign of PISNe among EMP stars.

Key words: galaxies: evolution — ISM: abundances — stars: formation — stars: low-mass — stars: Population III — stars: Population II

1 INTRODUCTION

The stellar initial mass function (IMF) and the evolution of elemental abundances within ~ 1 billion years after the Big Bang have been intensively investigated to uncover the nature of the early structure formation. The IMF and the metal content evolve, affecting each other. The first-generation stars (Pop III stars) born in pristine clouds are majorly massive ($\sim 100\text{--}1000 M_{\odot}$) by the lack of cooling agents other than hydrogen molecules (Bromm et al. 1999; Abel et al. 2002; Yoshida et al. 2003; Susa et al. 2014; Hirano et al. 2014, 2015a). They explode to enrich the surrounding gas with metals and dusts. The metal- and dust-enriched clouds undergo fragmentation by additional radiative cooling, and are likely to host low-mass stars (Pop II/I stars Omukai 2000; Schneider et al. 2003; Bromm & Loeb 2003; Frebel et al. 2005).

Those star formation and metal enrichment proceed in the early stage of the structure formation. The standard Λ cold dark matter (Λ CDM) model predicts that the structures hierarchically evolve from small to large ones, i.e., from stars to galaxies/galaxy clusters (Audouze & Silk

1995). Pop III stars are formed in tiny dark matter (DM) haloes with mass $M_{\text{halo}} \sim 10^6 M_{\odot}$ and with the virial temperature $T_{\text{vir}} \simeq 1000$ K, so-called minihaloes (MHs), at redshifts $z \sim 20$. Then, through the halo merger, the first galaxies, defined as objects in which the cycle of material stably stands, are formed in atomic-cooling haloes with $M_{\text{halo}} \sim 10^8 M_{\odot}$ at $z \sim 10$ (Bromm & Yoshida 2011). These objects are considered to contain more primitive population of stars and elemental abundances than those in the present-day massive galaxies. In the next decades, observational instruments such as the Thirty-Meter Telescopes (TMT), Space Infrared Telescope for Cosmology and Astrophysics (*SPICA*), and James-Webb Space Telescope (*JWST*) target the high-redshift galaxies, or even the first galaxies. The formation of galaxies at high redshifts have intensely been investigated by numerical simulations (e.g. Wise et al. 2012; Xu et al. 2013; Barrow et al. 2017a,b) and semi-analytical studies (e.g. de Bressan et al. 2014, 2017; Komiya et al. 2015; Magg et al. 2017). The confrontation of these simulations with the future observations will help us to understand the metal enrichment process in the early universe.

Another way to approach the stellar IMF and metal enrichment process in the early Universe is to observe long-lived metal-poor (MP) stars residing in the outskirts of our

* E-mail: chiaki@center.konan-u.ac.jp

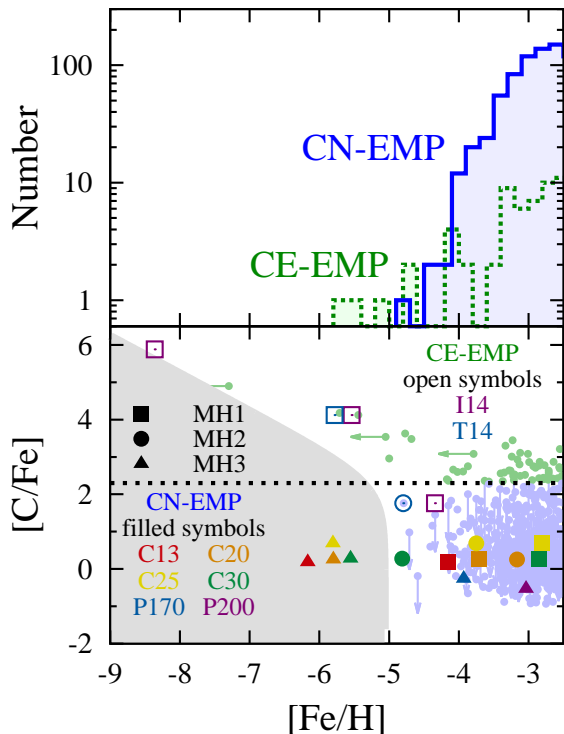


Figure 1. **Top:** Number distribution of CN-EMP (blue solid curve) and CE-EMP (green dotted) stars as a function of metallicity $[\text{Fe}/\text{H}]$. **Bottom:** Elemental abundance ratios of observed CN-EMP (blue dots) and CE-EMP (green) on the $[\text{C}/\text{Fe}]$ - $[\text{Fe}/\text{H}]$ plane retrieved by SAGA database (Suda et al. 2008, 2017). The horizontal black dotted line is the boundary between the two classes ($[\text{C}/\text{Fe}]_b = 2.30$), and gray shaded area is the region where the dust cooling efficiency is too small to trigger the low-mass star formation (Chiaki et al. 2017). The symbols denote our simulation results for MH1 (squares), MH2 (circles), and MH3 (triangles). The results in the progenitor models reproducing elemental abundances of CN-EMP and CE-EMP stars are denoted by filled and open symbols with the corresponding colours indicated by bottom-left and top-right corners of the panel, respectively (see text).

Galaxy and ultra-faint dwarf (UFD) galaxies. The metallicity of MP stars are often measured as iron abundance normalized by the solar one, $[\text{Fe}/\text{H}] = \log y(\text{Fe}) - \log y_{\odot}(\text{Fe})$, where $y(j)$ is the number abundance of element j relative to hydrogen nuclei. In particular, the stars with $[\text{Fe}/\text{H}] < -3$ are called as extremely metal-poor (EMP) stars, which are considered to be enriched by a single or several SN(e) for their small metal contents (Ryan et al. 1996; Cayrel et al. 2004). As Figure 1 shows, they are classified according to their carbon-enhancement as C-enhanced EMP (CE-EMP) and C-normal EMP (CN-EMP) stars above and below $[\text{C}/\text{Fe}]_b = 2.30$, respectively (Beers & Christlieb 2005; Aoki et al. 2007; Chiaki et al. 2017). It is considered that MP stars are originated from the fragmentation of their parent clouds by the radiative cooling of dust thermal emission so that the low-mass, i.e., long-lived stars are likely to be formed (Omukai 2000; Schneider et al. 2003, 2006; Bromm 2014). The distribution of CE-EMP and CN-EMP stars shows the vacant region on $[\text{C}/\text{Fe}]$ - $[\text{Fe}/\text{H}]$ plane (gray

shaded region), which would indicate the minimum elemental abundances $[\text{Fe}/\text{H}]_{\text{cr}} \sim -5$ and $[\text{C}/\text{H}]_{\text{cr}} \sim -3$ required to activate the carbon and silicate dust cooling, respectively (Chiaki et al. 2017).

The enrichment of the gas that will collapse to form EMP stars proceeds in qualitatively distinct ways. It is considered that there are two major processes, internal enrichment (IE) and external enrichment (EE). In the former case, SN shocks rich with metals fall back into and pollute the MH which has hosted a progenitor Pop III star. Ritter et al. (2012, 2015, 2016) and Sluder et al. (2016) find that, several ten million years after the explosion, the gas contracts again by the gravitational potential of the central MH, and the resulting metallicity is above $10^{-4} Z_{\odot}$. In the latter case, SN shocks from a MH reach and pollute neighbouring haloes. Smith et al. (2015) report that a neighbouring halo is enriched up to $2 \times 10^{-5} Z_{\odot}$ in a cosmological simulation. Besides, with the initial condition put by hand and higher resolution simulations, Chen et al. (2017) report that metal can not penetrate into the center of the clouds eroded by SN shocks for any models but for a model with a PISN. These simulations predict the lower metallicity in the second-generation star-forming regions than IE. We expect that the metallicity range depends on the enrichment processes.

Both IE and EE should occur, depending on the balance between the injected energies of ultraviolet photons/SN explosions and the halo binding energy. Therefore, to know the conditions for the two enrichment processes and which process is dominant, it is required to perform simulations in a wide range of parameters such as masses of MH M_{halo} and a Pop III star M_{PopIII} . However, IE and EE have so far been separately investigated with one combination of the initial parameters by each earlier work.

In addition, the elemental abundance of EMP stars is the clue to restrict IMF of Pop III stars. Pop III stars with masses $8 M_{\odot} < M_{\text{PopIII}} < 40 M_{\odot}$ explode as normal Type-II core-collapse SNe (CCSNe) and eject the normal elemental abundance ratio. More massive ones with $140 M_{\odot} < M_{\text{PopIII}} < 260 M_{\odot}$ explode as pair-instability SNe (PISNe) and their ejecta show Fe-enhanced features and the large abundance contrasts between odd and even elements (Aoki et al. 2014). The elemental abundances of EMP stars can well be reproduced by the nucleosynthetic models of CCSNe. Interestingly, the stars with elemental abundances consistent with PISN model have not been observed so far. This is considered to be either because the formation rate of extremely massive Pop III stars are intrinsically small, or because the ejecta from PISNe, if exist, can not enrich their host or neighbouring MHs. Again, most of earlier works employ one initial parameter of M_{PopIII} , and restrict their interest to either CCSNe or PISNe. To compare with the observations, the simulations with M_{PopIII} covering the mass ranges from CCSNe to PISNe is required.

Another clue of the nucleosynthetic feature of Pop III stars is that CE-EMP stars account for the dominant fraction (80%) for the subset of EMP stars with lowest metallicity ($[\text{Fe}/\text{H}] < -4.5$). Their origin is considered to be the enrichment of their parent clouds by faint SNe (FSNe) whose inner layer of ejecta undergoes mixing/fall-back and only C-rich materials are ejected (Umeda & Nomoto 2003; Marassi et al. 2014, 2015; Chen et al. 2017; Chiaki et al.

2017). Although the model can well reproduce the relative elemental abundance of CE-EMP stars, it has not yet been explicitly shown that the absolute elemental abundance of enriched clouds becomes as high as observed values of $[C/H] \sim -3$ regardless of the loss of the ejecta mass.

We in this paper focus on the first step of the matter cycle from the formation of Pop III stars to star-forming clouds of Pop II stars. We perform a series of simulations to study the metal enrichment of star-forming clouds by a single Pop III star, considering its radiative/mechanical feedbacks. The method is described in Section 2. We investigate two environmental parameters: masses of MHs with a range of $M_{\text{halo}} = 3 \times 10^5 - 3 \times 10^6 M_{\odot}$ and Pop III stars $M_{\text{PopIII}} = 13 - 200 M_{\odot}$, covering the mass range of CCSNe and PISNe. The results of the simulations separately for the combination of massive/low-mass MHs and CCSNe/PISNe are shown in Section 3. We find the different ‘modes’ appear in the enrichment processes as discussed in Section 4, and apply our result to the comparison with observations of EMP stars (Section 5). We discuss other issues in Section 6, and conclude the paper in Section 7.

2 NUMERICAL MODELS

2.1 Flow of simulations

This work follows the process of radiative feedback from main-sequence (MS) Pop III stars and kinetic feedback and metal dispersion from their SNe. Throughout the simulations, we employ the N -body/Smoothed Particle Hydrodynamics (SPH) code GADGET-2 (Springel 2005) including all relevant non-equilibrium chemistry and heating/cooling processes. The whole course of the simulations is divided into the following three steps.

Formation of minihaloes and Pop III stars

We extract MHs from a parent cosmological simulation with a large simulation box, and calculate gravitational collapse of Pop III star-forming clouds hosted by MHs until the central density reaches $n_{\text{H, cen}} = 10^3 \text{ cm}^{-3}$ and run-away collapse onsets.

Radiative feedback

After the collapse simulations, we put a collisionless particle as a Pop III star at the centroid of SPH particles with densities $n_{\text{H}} > n_{\text{H, cen}}/3$. The velocity of the star particle is initially mass-weighted average of the central SPH particles. We update it by integrating the gravity force. The star particle is the source of ionization and dissociation photons. According to their mass, the emission rates of ionizing and dissociating photons are given. After the corresponding lifetime of a Pop III star, the photon emission is turned off to give the initial condition of the subsequent simulations of SN explosions.

Supernova feedback

Then, propagation of shock front associated with the supernova explosion is followed under the point explosion approximation. All of the energies are added as thermal energy at the location of the Pop III star particle. The energy is given according to the different types of SN, CCSNe and

PISNe. We follow the metal dispersion until the density of the recollapsing region reaches $n_{\text{H, cen}} = 10^3 \text{ cm}^{-3}$ again.

2.2 Resolution

In an SPH scheme, a density distribution is expressed as the spatial distribution of SPH particles. As the nature of the scheme, the spatial resolution is automatically improved with increasing density. The employed mass of an SPH particle is $m_{\text{p}}^{\text{gas}} = 4.45 M_{\odot}$ and the number of neighbouring particles is $N_{\text{ngb}} = 64$. As a result, the minimum mass which SPH particles resolve is $M_{\text{min}} = N_{\text{ngb}} m_{\text{p}}^{\text{gas}}$. For the maximum density $n_{\text{H, max}}$, the minimum length which can be resolved is described as the minimum smoothing kernel size,

$$h_{\text{min}} = 1.3 \text{ pc} \left(\frac{N_{\text{ngb}}}{64} \right)^{1/3} \left(\frac{m_{\text{p}}^{\text{gas}}}{4.45 M_{\odot}} \right)^{1/3} \left(\frac{n_{\text{H, max}}}{10^3 \text{ cm}^{-3}} \right)^{-1/3}. \quad (1)$$

However, when the size fails to sufficiently resolve the local Jeans length, it is reported that spurious fragmentation occurs (Truelove et al. 1997). At the maximum density, the ratio \mathcal{R}_{cr} of the local Jeans mass M_{J} to M_{min} is

$$\mathcal{R}_{\text{cr}} = \frac{M_{\text{J}}}{M_{\text{min}}} = 18 \left(\frac{N_{\text{ngb}}}{64} \right)^{-1} \left(\frac{m_{\text{p}}^{\text{gas}}}{4.45 M_{\odot}} \right)^{-1} \times \left(\frac{n_{\text{H}}^{\text{max}}}{10^3 \text{ cm}^{-3}} \right)^{-1/2} \left(\frac{T}{300 \text{ K}} \right)^{2/3} \quad (2)$$

(Chiaki & Yoshida 2015). In simulations of isolated collapsing gas clouds, the ratio \mathcal{R}_{cr} is obliged to be above 1000 by zoom-in techniques such as the particle-splitting (Hirano et al. 2014; Chiaki et al. 2016). In our simulations, the minimum resolution of $\mathcal{R}_{\text{cr}} = 18$ is sufficient because we are not interested in the cloud fragmentation but the average metallicity of recollapsing region.

2.3 Chemical reactions and heating/cooling

2.3.1 Non-radiative reactions

Throughout the simulation, we solve the non-equilibrium chemical networks of 53 reactions for 15 primordial species of e, H, H^+ , H_2 , H^- , H_2^+ , HeH^+ , He, He^+ , He^{2+} , D, D^+ , D^- , HD, and HD^+ , which cover the wide range of density of $10^{-3} \text{ cm}^{-3} < n_{\text{H}} < 10^5 \text{ cm}^{-3}$ and temperature of $100 \text{ K} < T < 10^9 \text{ K}$. The collisional ionization and recombination of H and He atoms and ions, charge transfer of relevant species, and formation of H_2 and HD molecules are included. The compilation of reaction rates is taken from the primordial part of Nagakura et al. (2009).

2.3.2 Radiative cooling

From abundances of the species, we calculate the radiative cooling rates of the inverse Compton cooling, bremsstrahlung, H, He, and He^+ transition lines including two-photon decay, ionization and recombination cooling, and ro-vibrational transition line cooling of H_2 and HD molecules. We do not include the radiative cooling by ejected metal because it activates at densities $n_{\text{H}} \gtrsim 10^3 \text{ cm}^{-3}$ with metallicities $Z \gtrsim 10^{-3} Z_{\odot}$, above our maximum density (Jappsen et al. 2007).

We ignore the star formation in neighbouring haloes, focusing on the enrichment of one halo which have hosted the Pop III star. In order to prevent the gas from collapsing in the neighbouring haloes, H_2 and HD cooling is switched off in the region 100 pc outside from the target halo, the typical virial radius. Inside 100 pc from the center of the target halo, we prevent density from increasing larger than $n_{\text{H,cen}} = 10^3 \text{ cm}^{-3}$ by switching off molecular cooling due to the limit of resolution.

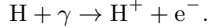
2.3.3 Photo-chemistry and heating

Radiative transfer

During MS of Pop III stars, we perform radiation transfer simulations, using the ray-tracing method presented by Susa (2006). The rates of photoionization and dissociation are calculated at the position of each SPH particle. Since they depend on the column density of the relevant species, we derive this by integrating the element $\Delta N_i(\text{H I})$ along the ray from the source to the target SPH particle. The element $\Delta N_i(\text{H I})$ is calculated between a SPH particle i on the ray and one of its neighbors j that is selected so that the angle between the direction from i to j and the direction from i to the source is smallest. The subroutine of radiative transfer are heavily parallelized.

Photoionization of H atoms

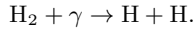
We add the reactions of photoionization of H atoms and photodissociation of H_2 molecules. The former proceeds by the ionizing photons with energies $h\nu > h\nu_{\text{L}} = 13.6 \text{ eV}$ as



The reaction rate $k_{\text{ion},i}$ and corresponding heating rate $\Gamma_{\text{ion},i}$ at the position of an SPH particle i are calculated from the column density $N_i(\text{H I})$, using the photon-conserving procedure (Susa 2006). The frequency-dependent cross-section σ_ν is taken from Shapiro & Kang (1987). We ignore the photoionization of helium atoms and ions.

Photodissociation of H_2 molecules

The dissociation of hydrogen molecules induced by photons in the Lyman-Werner band (11.2–13.6 eV) are also solved as



Using the self-shielding approximation of Draine & Bertoldi (1996), we calculate the photodissociation rate by the column density of H_2 molecules.

2.4 Supernova Feedback

2.4.1 Mechanical feedback

The explosion energy is added as thermal energy uniformly in a spherical region around a Pop III remnant which contains $N_{\text{FE}} = 200$ gas particles, mimicking the end of the free-expansion (FE) phase. Note that the FE phase is transmitted into the Sedov-Taylor (ST) phase when a SN ejecta sweeps up the ambient medium with the same mass. Since the mass of SPH particles is $m_{\text{p}}^{\text{gas}} \sim 5 M_{\odot}$ in this simulation, the mass of the initial heated region is $N_{\text{FE}} m_{\text{p}}^{\text{gas}} \sim 1000 M_{\odot}$, which is larger than the ejecta mass. It is the trade-off for the

Table 1. Properties of minihaloes

	MH	z_{col}	$R_{\text{halo}}^{\text{col}}$ [pc]	$M_{\text{halo}}^{\text{col}}$ [M_{\odot}]	$M_{\text{pri}}^{\text{col}}$ [M_{\odot}]
LH	MH1	28.47	70.12	2.94×10^5	3.91×10^4
	MH2	27.52	79.52	3.89×10^5	5.26×10^4
HH	MH3	23.58	186.85	3.23×10^6	4.80×10^5

Note — $M_{\text{halo}}^{\text{col}}$ and $R_{\text{halo}}^{\text{col}}$ denote the virial mass and radius of MHs so that the average density of both gas and dark matter is 200 times the critical density at the redshift z_{col} when the maximum gas density reaches $n_{\text{H,cen}}^{\text{col}} = 10^3 \text{ cm}^{-3}$. $M_{\text{pri}}^{\text{col}}$ is the gas mass within $R_{\text{halo}}^{\text{col}}$.

large simulation box size of $\sim \text{kpc}$ to cover the entire volume which PISN shell can cover. Zoom-in techniques such as particle splitting (Chiaki & Yoshida 2015) could resolve the innermost region of SN ejecta. However, when refined particles are brown away into the ambient region with coarse gas particles, significant error in density and pressure force estimations would be induced. Thus, we do not employ the particle splitting in the present simulations.

2.4.2 Metal enrichment

The propagation of metals is traced by Lagrangian test particles with mass $m_{\text{p}}^{\text{met}} = M_{\text{met}}^{\text{ej}}/N_{\text{met}}$, where $M_{\text{met}}^{\text{ej}}$ is the metal mass produced by SNe and N_{met} is the number of metal particles. We set $N_{\text{met}} = 10^5$ as in Ritter et al. (2012). The velocity \mathbf{v} of a metal particle i is interpolated from neighbouring SPH particles j with the ordinal SPH procedure as

$$\mathbf{v}_i = \sum_j \frac{m_j}{\rho_j} \mathbf{v}_j W(r_{ij}, h_i), \quad (3)$$

where m_j , ρ_j , and \mathbf{v}_j denote the mass, density, and velocity of SPH particle j , r_{ij} is the distance between the metal particle i and SPH particle j , h_i is the smoothing length of metal particle i within which N_{ngb} SPH particles are contained, and $W(r, h)$ is the smoothing kernel function. Then the position \mathbf{x}_i of a metal particle i at the time t are updated as $\mathbf{x}_i(t + \Delta t) = \mathbf{x}_i(t) + \mathbf{v}_i(t)\Delta t$, where Δt is the simulation timestep.

Note that we here employ the ordinal cubic spline kernel to estimate metal density of each SPH particle. In order to obtain a better estimation of metallicity, some researchers adopt various kernel functions (Tornatore et al. 2007a,b; Dehnen & Aly 2012). Tornatore et al. (2007b) compare the runs with the ordinal cubic spline and top-hat kernel function. They conclude that the difference of metallicity between two runs are less significant relative to the diversity of realizations. Thus we employ the ordinary cubic spline kernel function.

2.4.3 Metallicity in recollapsing region

The metallicity of the recollapsing region is calculated as

$$Z_{\text{cen}}^{\text{recol}} = \frac{M_{\text{met,cen}}^{\text{recol}}}{M_{\text{pri,cen}}^{\text{recol}} + M_{\text{met,cen}}^{\text{recol}}}, \quad (4)$$

Table 2. Properties of Pop III stars

	ID	M_{PopIII} [M_{\odot}]	${}^a t_{\text{life}}$ [Myr]	${}^a T_{\text{eff}}$ [K]	${}^a Q(\text{H})$ [s^{-1}]	${}^b E_{\text{SN}}$ [10^{51} erg]	${}^b M_{\text{met}}^{\text{ej}}$ [M_{\odot}]	${}^b M_{\text{Fe}}^{\text{ej}}$ [M_{\odot}]
CCSN	C13	13	13.7	5.22×10^4	1.33×10^{48}	1	0.746	0.0718
	C20	20	8.43	6.41×10^4	4.72×10^{48}	1	2.56	0.0789
	C25	25	6.46	7.08×10^4	7.58×10^{48}	1	3.83	0.0758
	C30	30	5.59	7.37×10^4	1.33×10^{49}	1	7.18	0.105
PISN	P170	170	2.32	9.83×10^4	2.16×10^{50}	20	83.4	4.42
	P200	200	2.20	9.98×10^4	2.62×10^{50}	28	114	7.74

References — *a.* The quantities are linearly interpolated from table 4 of Schaerer (2002); *b.* Umeda & Nomoto (2002)

where $M_{\text{met,cen}}^{\text{recol}}$ and $M_{\text{pri,cen}}^{\text{recol}}$ are the mass of metal and primordial gas particles within the local Jeans radius centered at the SPH particle of highest density. From the total ejected mass $M_{\text{Fe}}^{\text{ej}}$ of Fe, we can estimate the number abundance $y_{\text{cen}}^{\text{recol}}(\text{Fe})$ of Fe relative to hydrogen in the recollapsing region as

$$y_{\text{cen}}^{\text{recol}}(\text{Fe}) = \frac{Z_{\text{cen}}^{\text{recol}} M_{\text{Fe}}^{\text{ej}}}{\mu_{\text{Fe}} X_{\text{H}} M_{\text{met}}^{\text{ej}}}, \quad (5)$$

where $\mu_{\text{Fe}} = 56$ is the molecular weight of Fe. Using the solar abundance $A_{\odot}(\text{Fe}) = 12 + \log[y_{\odot}(\text{Fe})] = 7.50$ (Asplund et al. 2009), the relative abundance is estimated as $[\text{Fe}/\text{H}]_{\text{cen}}^{\text{recol}} = \log[y_{\text{cen}}^{\text{recol}}(\text{Fe})/y_{\odot}(\text{Fe})]$.

2.5 Initial conditions

2.5.1 Minihaloes

In the parent cosmological simulation, we use GADGET-2 suitably modified to follow the formation of primordial gas clouds (Hirano et al. 2014). The simulations are initialized at $z_{\text{ini}} = 99$ with a box size $10 h^{-1}$ Mpc using the MUSIC software (Hahn & Abel 2011). Cosmological parameters are adopted from the latest Planck data (Planck Collaboration et al. 2016, last column of their table 4). We first run a dark matter only simulation with 512^3 N -body particles, and identify dark haloes at $z = 10$ by running a friends-of-friends halo finder. Next, we perform multi-level zoom-in simulations for the selected target haloes with a high spatial resolution. Finally, we perform the zoom-in simulations including SPH particles with mass $m_{\text{p}}^{\text{gas}} \sim 0.3 M_{\odot}$. The SPH simulations are stopped when the target haloes collapse gravitationally, and the central gas density reaches $n_{\text{H}} = 10^3 \text{ cm}^{-3}$. We select three MHs with masses 3×10^5 – $3 \times 10^6 M_{\odot}$ to cover the mass range of MHs in the entire cosmological MHs given by Hirano et al. (2015a). We step back the simulation when the central gas density is $n_{\text{H}} = 1 \text{ cm}^{-3}$, and cut out a spherical region with a radius 2.5 kpc centered at the density peak so that the SN shocks even for PISNe can not go beyond the simulation region. We then restart the collapse simulation with the chemical reactions and radiative cooling presented in Section 2.3.

Table 1 shows the total mass $M_{\text{halo}}^{\text{col}}$ and baryon mass $M_{\text{pri}}^{\text{col}}$ within the virial radius $R_{\text{halo}}^{\text{col}}$ of the MHs at the time when their maximum density reaches 10^3 cm^{-3} for the first time. MH1 and MH2 host Pop III stars at high redshifts 27–28. The mass of both MH1 and MH2 is around $3 \times 10^5 M_{\odot}$,

but MH1 does not have substructures within 500 pc around it while MH2 does. Until the time when shocked gas falls back into MH2, it is expected that the neighbouring haloes also merge with MH2 and reduce its metallicity. We also study the enrichment of more massive halo, MH3, with $3 \times 10^6 M_{\odot}$ growing at a lower redshift 24.

2.5.2 Pop III stars

The mass function of Pop III stars is still under the debate because of the limitations of spatial resolution and computational time to follow the entire accretion history of a disk into the central protostellar core. Several researchers have reported that the fragmentation of accretion disk around a protostar drives the formation of Pop III star cluster including low-mass ($\lesssim 1 M_{\odot}$) stars (Clark et al. 2011; Greif et al. 2011; Stacy et al. 2012; Susa 2013; Susa et al. 2014; Chiaki et al. 2016; Hirano & Bromm 2017). However, even in such simulations, the primary protostar is still massive ($\gtrsim 10 M_{\odot}$). In the present simulations we only take into account the feedback by a primary star.

We consider the wide range of progenitor mass of $M_{\text{PopIII}} = 13$ – $30 M_{\odot}$ and 170 – $200 M_{\odot}$ exploding as CC-SNe and PISNe. These models reproduce the elemental abundance ratio of CN-EMP stars. The stellar properties, such as their lifetime t_{life} and emission rate of ionizing photons $Q(\text{H})$, are interpolated by the quantities presented by Schaerer (2002) as listed in Table 2. The explosion energy E_{SN} is fixed for CCSNe to be 1×10^{51} erg, and 20×10^{51} and 28×10^{51} erg for PISNe with $M_{\text{PopIII}} = 170$ and $200 M_{\odot}$, respectively. With those explosion energies, the mass $M_{\text{met}}^{\text{ej}}$ of nucleosynthesized metal is listed in Table 2 (Umeda & Nomoto 2002). The mass of synthesized iron $M_{\text{Fe}}^{\text{ej}}$ is less sensitive to the progenitor mass than the total metal mass. The oxygen mass accounts for the large fraction of the ejected metal, and increases with M_{PopIII} , but it is observationally difficult to constrain the oxygen abundance of EMP stars (Cayrel et al. 2004).

Hereafter, we indicate these models by the combination of IDs of MHs and M_{PopIII} . The name ‘MH1-C30’ denotes the model with $M_{\text{PopIII}} = 30 M_{\odot}$ hosted in MH1, for example. For the later discussion, we generalize the models with $13 M_{\odot} \leq M_{\text{PopIII}} \leq 30 M_{\odot}$ as ‘CCSN’ and $170 M_{\odot} \leq M_{\text{PopIII}} \leq 200 M_{\odot}$ as ‘PISN’. Also, we call low-mass MH1 and MH2 as LH while high-mass MH3 as HH to compare their hydrodynamic evolutions.

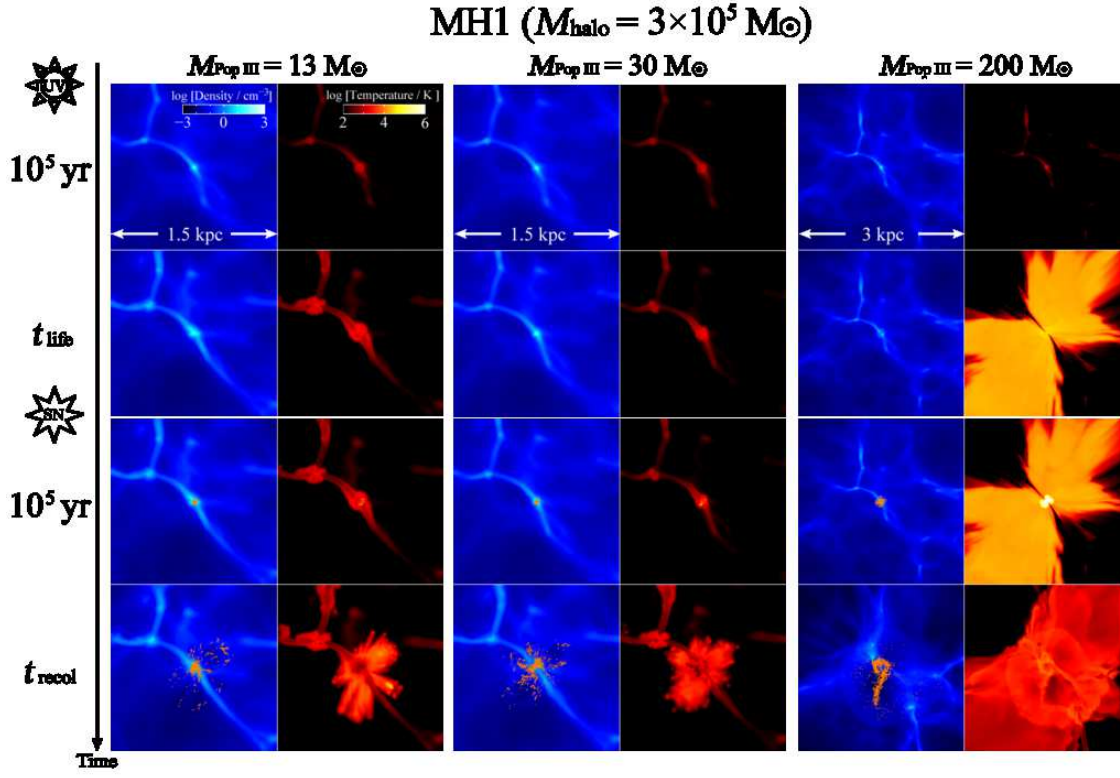


Figure 2. Density (left panels) and temperature (right) slices for MH1 at 10^5 yr after star formation, the life time of Pop III stars t_{life} , 10^5 yr after SN explosion, and the time when gas recollapses t_{recol} (from top to bottom rows). The physical box size is indicated in the first row. The orange dots overlapped on the density maps represent the position of metal particles close to the slicing plane within 2.5 times their kernel size.

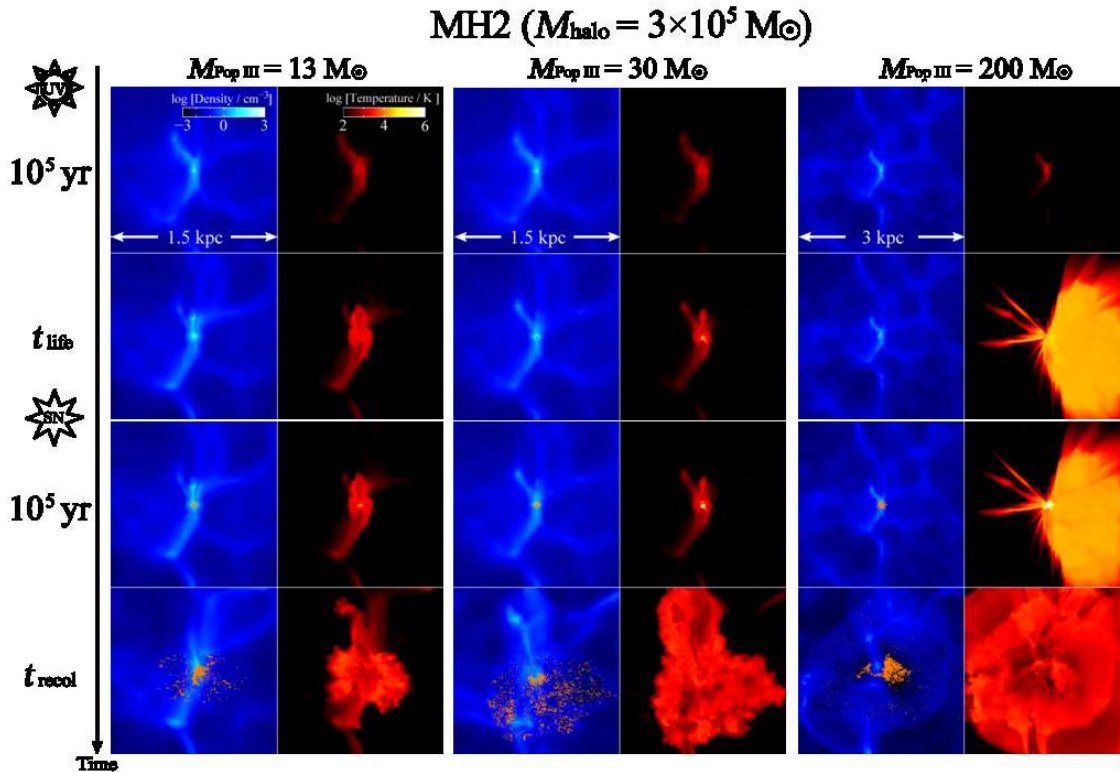


Figure 3. Same as Figure 2 but for MH2.

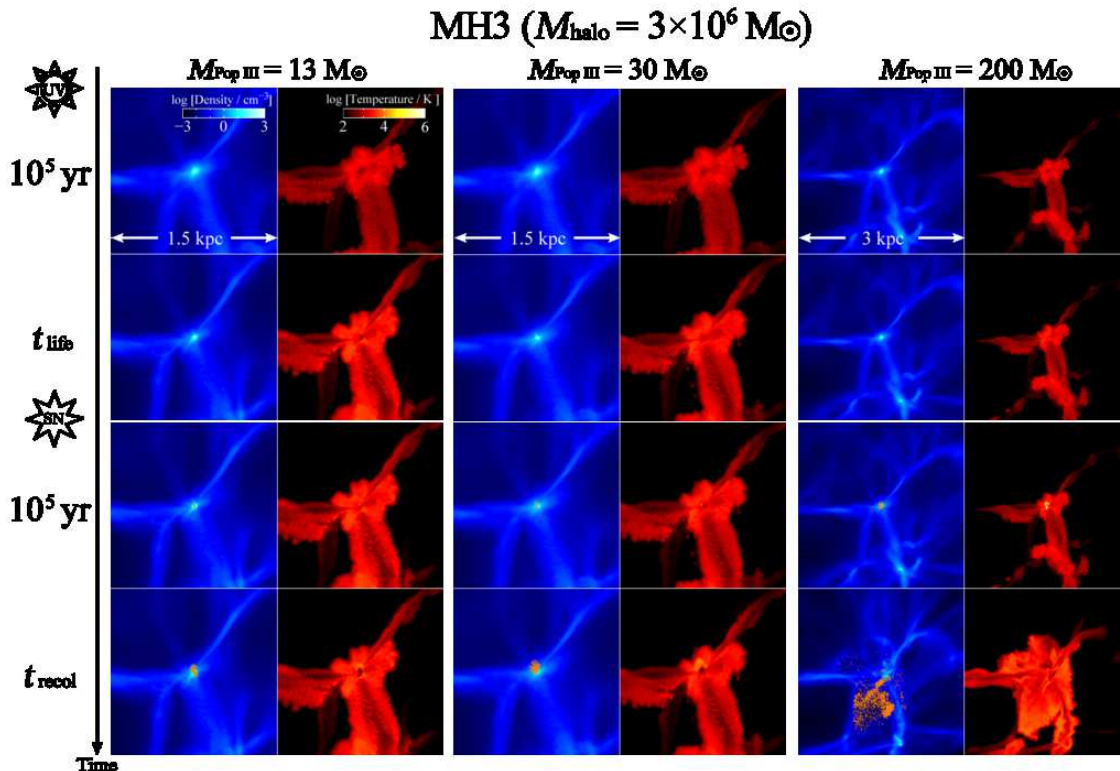


Figure 4. Same as Figure 2 but for MH3.

2.5.3 Parameters of the Cosmological Simulation

Throughout the simulations as well as the parent cosmological simulation, the cosmological parameters are $\Omega_m = 0.31$, $\Omega_b = 0.047$, $\Omega_\Lambda = 0.69$, and $H_0 = 100 h = 68 \text{ km s}^{-1} \text{ Mpc}^{-1}$ (Planck Collaboration et al. 2016). We perform simulations in the comoving coordinate, but we show the physical quantities in proper coordinate in the text, tables, and figures hereafter.

Although helium is nucleosynthesized and dispersed by a SN, we fix the mass fraction of helium to $Y_{\text{He}} = 0.24$. We show gas density in the form of number density of hydrogen nuclei as $n_{\text{H}} = X_{\text{H}}\rho/m_{\text{H}}$, where $X_{\text{H}} = 1 - Y_{\text{He}}$ is the mass fraction of hydrogen nuclei, ρ is the mass density of gas, and m_{H} is the mass of a hydrogen nucleus. The metallicity is shown in the unit of the solar one $Z_{\odot} = 0.02$.

3 RESULTS

3.1 Overview

Figures 2–4 show the density and temperature distributions during MS (top two rows) and after SN explosions (bottom two rows) for each MH. In most models, the central gas clouds hosted by MHs are not affected or partly broken by the emission of ionizing photons. Then, after SN explosions, metal particles expel mainly in the direction perpendicular to the filaments of the cosmological large-scale structures, i.e., direction to the voids. A fraction of metals is halted to be dispersed by the continuous gas accretion in the direction of the filament, and falls back into the central MHs at 1–10

Myr after explosions. The MHs are self-enriched (IE) by Pop III stars which they have hosted (Figure 5). The metallicity ranges in the recollapsing clouds are $Z_{\text{cen}}^{\text{recol}} \sim 10^{-4}$ – $10^{-2} Z_{\odot}$ for LH, consistent with that of observed EMP stars, and 10^{-6} – $10^{-5} Z_{\odot}$ for HH as shown in Figure 6 and Table 3. The metallicity of recollapsing regions depends not only on the halo mass and the Pop III mass, but also on the presence of substructures. When subclumps merge before the run-away collapse of the recollapsing cloud, the pristine gas flows into the central clouds, and the metallicity becomes smaller than in the cases without substructures.

On the other hand, for LH-PISN, H II regions expel to more than 1 kpc away from the central Pop III stars as indicated by the region with several tens-thousands kelvins. The gas with metals is ejected from SNe and never falls back until at least 50 Myr after SN. Instead, it goes through the voids to reach the regions within virial radii of several neighbouring haloes locating at ~ 1 kpc distant from the central MHs (Figures 2 and 3). We observe that metals are incorporated into the central part of one neighbouring halo, and its metallicity is $\lesssim 10^{-6} Z_{\odot}$, indicating that EE is ineffective relative to IE.

The metallicity ranges in the recollapsing regions depend largely on enrichment processes, IE or EE. We can see this for the first time by performing simulations for ranges of M_{halo} and $E_{\text{SN}} (M_{\text{Pop III}})$. We see the details of hydrodynamical evolution and resulting metallicity range of the recollapsing regions for IE (Section 3.2) and EE events (Section 3.3).

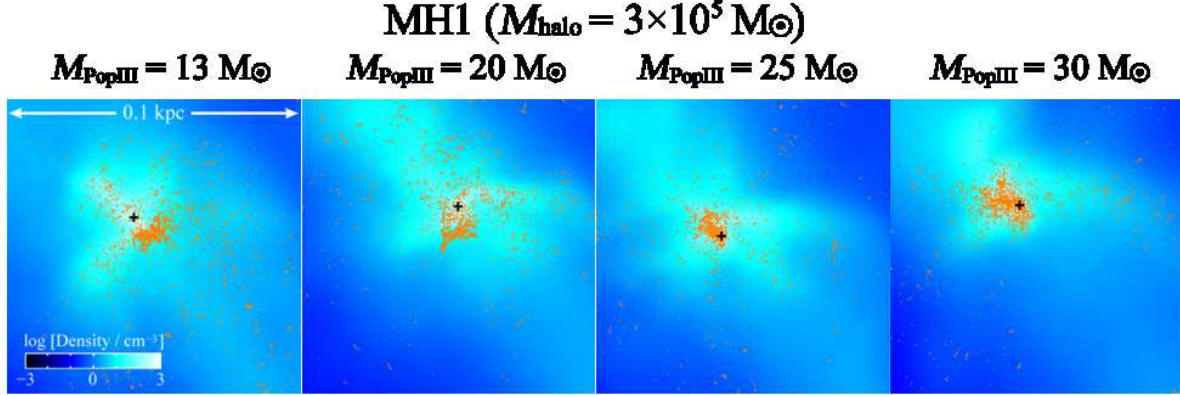


Figure 5. Central part of Figure 2 at the time t_{recol} after SN explosions with progenitor masses $M_{\text{PopIII}} = 13\text{--}30 M_{\odot}$ for MH1 with a box size 0.1 kpc around the explosion center. The plus symbols and orange dots indicate the positions of the gas density peak and metal particles, respectively.

Table 3. Properties and metallicities of self-enriched haloes

Halo	M_{PopIII} [M_{\odot}]	$n_{\text{H,cen}}^{\text{life}}$ [cm^{-3}]	t_{recol} [Myr]	$Z_{\text{cen}}^{\text{recol}}$ [Z_{\odot}]	$[\text{Fe}/\text{H}]_{\text{cen}}^{\text{recol}}$	$f_{\text{halo}}^{\text{met}}$	$f_{\text{halo}}^{\text{pri}}$	$Z_{\text{halo}}^{\text{recol}}$ [Z_{\odot}]
MH1	13	3.14×10^2	5.74	4.89×10^{-5}	-4.16	0.555	3.87	1.37×10^{-4}
	20	7.16×10^2	7.19	4.22×10^{-4}	-3.71	0.459	2.85	5.28×10^{-4}
	25	2.66×10^2	8.41	5.31×10^{-3}	-2.81	0.368	2.60	6.94×10^{-4}
	30	1.62×10^1	12.2	6.62×10^{-3}	-2.84	0.398	2.62	1.39×10^{-3}
MH2	13	8.31×10^1	11.3	4.88×10^{-5}	-4.16	0.701	3.79	1.31×10^{-4}
	20	5.90×10^0	12.5	1.49×10^{-3}	-3.17	0.648	2.90	5.44×10^{-4}
	25	6.09×10^1	22.4	6.03×10^{-4}	-3.75	0.300	4.07	2.68×10^{-4}
	30	1.39×10^0	39.7	7.10×10^{-5}	-4.81	0.254	5.96	2.91×10^{-4}
MH3	13	9.02×10^5	0.979	4.77×10^{-7}	(-6.17)	0.895	1.91	3.63×10^{-5}
	20	7.88×10^5	1.16	3.48×10^{-6}	(-5.80)	0.608	1.31	1.24×10^{-4}
	25	7.31×10^5	1.23	5.33×10^{-6}	(-5.80)	0.557	1.32	1.68×10^{-4}
	30	4.77×10^5	1.30	1.29×10^{-5}	(-5.55)	0.421	1.30	2.43×10^{-4}
	170	6.30×10^2	5.85	1.49×10^{-4}	-3.93	0.368	1.17	2.73×10^{-3}
	200	2.96×10^1	28.5	9.10×10^{-4}	-3.04	0.449	2.94	1.83×10^{-3}

Note — (3) $n_{\text{H,cen}}^{\text{life}}$: central number density at the lifetime of a Pop III star. (4) t_{recol} : time to recollapse from a SN explosion. (5, 6) $Z_{\text{cen}}^{\text{recol}}$, $[\text{Fe}/\text{H}]_{\text{cen}}^{\text{recol}}$: metallicity and iron abundance in the recollapsing cloud. Parentheses are attached for models with $[\text{Fe}/\text{H}]_{\text{cen}}^{\text{recol}}$ below the critical value $[\text{Fe}/\text{H}]_{\text{cr}} = -5$ (Chiaki et al. 2015, 2017). (7) $f_{\text{halo}}^{\text{met}}$: mass fraction of metal remaining within the virial radius R_{vir} to ejected. (8) $f_{\text{halo}}^{\text{pri}}$: mass fraction of primordial gas within R_{vir} at t_{recol} to the initial. (9) $Z_{\text{halo}}^{\text{recol}}$: metallicity within R_{vir} at t_{recol} .

3.2 Internal Enrichment

We observe IE for all models but for LH-PISN. Figure 7 shows the radial density profiles (a) during MS and (b) after SN explosions centered at Pop III stars and their explosion center, respectively. Radial profiles in two representative directions are shown by the solid and dotted curves that correspond to the directions to cosmological filaments and voids, respectively. The dynamics of the gas in the halo and the metallicity in the recollapsing region depend on M_{PopIII} , M_{halo} , and the presence substructures. We classify our models into three groups of LH-CCSN (Section 3.2.1), HH-CCSN (Section 3.2.2), and HH-PISN (Section 3.2.3). We summarize the complicated dependency of metallicity on M_{halo} and M_{PopIII} in Section 3.2.4.

3.2.1 CCSNe in Low-mass MHs

In the direction of filaments, H II regions is still R-type at 10^6 yr after star formation, and then transit to the D-type at t_{life} finding the D-type shocks at 1–10 pc from the Pop III stars for LH (solid yellow and orange curves in Figure 7). In the direction of voids, D-type fronts propagate more rapidly, reaching ~ 20 pc at t_{life} . The distance of the shocks from Pop III star increases with increasing M_{PopIII} because the emission rates of ionizing photons increases (Table 2). For MH1-C30 and MH2-C30, ionization region expands to 5 and 10 pc, and the density at the position of the Pop III star decreases from the initial value of $n_{\text{H,cen}}^{\text{col}} = 10^3 \text{ cm}^{-3}$ to $n_{\text{H,cen}}^{\text{life}} = 16.2$ and 1.39 cm^{-3} , respectively. On the other hand, for MH1-C13 and MH2-C13, the gas density only slightly decreases to 314 and 83.2 cm^{-3} , respectively. As the Pop

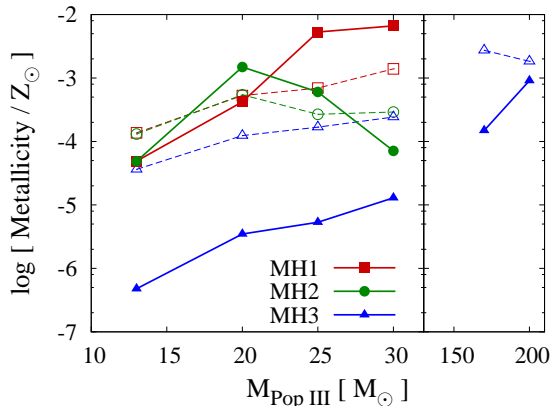


Figure 6. Metallicity in the recollapsing region as a function of the Pop III stellar mass for MH1 (red curves), MH2 (green), and MH3 (blue). The solid and dashed curves show the average metallicity within the Jeans length and virial radius, respectively.

III stellar mass decreases, the decrement of $n_{\text{H, cen}}^{\text{life}}$ becomes smaller because the ionization photon emission rate declines, and also because the halo mass becomes larger due to accretion through the longer stellar life time.

The blast wave from SN explosion further destroy the clouds in the MHs (Figure 7b). At $t \sim 10^6$ yr after explosion, the central region is significantly evacuated with densities less than $< 0.01 \text{ cm}^{-3}$. As shown in the fourth column of Table 3, the density of the recollapsing regions reaches 10^3 cm^{-3} at the time $t_{\text{recol}} = 5\text{--}40$ Myr after the explosion. The time t_{recol} becomes longer with increasing M_{PopIII} because the shock velocity decreases going through the denser region owing to weaker pre-ionization rates. Although about a half of metals is dispersed in the direction of voids (orange dots in Figure 2), the rest remains around the loci of the explosion center (Figure 5).

As shown in the last column in Table 3 and Figure 6, the metallicity in the recollapsing region is $5 \times 10^{-5} Z_{\odot} < Z_{\text{cen}}^{\text{recol}} < 7 \times 10^{-3} Z_{\odot}$ and $-4.16 < [\text{Fe}/\text{H}]_{\text{cen}}^{\text{recol}} < -2.84$, which indicates that the second generation stars are expected to form in the enriched clouds, to be found as EMP stars in the local Universe. We conclude that a single CCSN is enough to pollute the halo having hosted its progenitor to reproduce the metallicity range of the star-forming clouds of EMP stars.

The metallicity becomes smaller as the progenitor mass gets smaller. We find the enrichment process is different between large and small M_{PopIII} . As shown in Figure 5, for MH1-C25 and C30, the shocked gas contracts again, gathering metals remaining at the central region. On the other hand, for C13 and C20, the gas in the direction of the filament is compressed and begins to collapse too rapidly to fall back again into the center because the gas has been dense during MS due to the weak ionization efficiency. As Chiaki et al. (2013) predict by one-dimensional calculations, SN shells become gravitationally unstable during expanding in the dense medium. Since the metals coming from behind the shock can not efficiently penetrate into the shock-driven recollapsing region, the only slightly enriched cloud is formed in the offset region against the explosion center. We call the

former enrichment process as the *central recollapse*, and the latter as the shock-driven *off-central recollapse*.

Figure 8 shows the density and metallicity as a function of the distance from the density maxima of the recollapsing clouds at the time t_{recol} . For MH1-C13 (red curve), the metallicity is $\simeq 5 \times 10^{-5} Z_{\odot}$ in the center while it is higher ($\simeq 2 \times 10^{-4} Z_{\odot}$) at the distance ~ 10 pc, which indicates that metal does not penetrate into the off-center recollapsing region. On the other hand, for C30 (green curve), the metallicity is higher in the center than in the ambient gas, which indicates that metal is sufficiently incorporated into the central part of the recollapsing clouds. The slope of metallicity against the radius continuously becomes opposite with increasing M_{PopIII} from red to green curves for MH1 and from red to orange curves for MH2 in Figure 8.

We can not see this trend for MH2-C25 and C30. In those cases, a neighbouring halo containing only the pristine gas merges with the central halo from above in Figure 3. For C30, the neighbouring halo goes through the central one with a part of primordial gas accreted (Figure 3). Consequently, the metallicity for C25 and C30 is 6.03×10^{-4} and $7.10 \times 10^{-5} Z_{\odot}$, respectively, below the one for C20. The presence of substructures in the MHs can lead to the scatter of metallicity by two orders of magnitude.

Besides, for MH2-C13 and C20, the neighbouring halo approaches the central MH, but they do not merge until the central MH recollapses because t_{recol} is shorter for the less efficient photoionization than C25 and C30. The resulting metallicities with the same M_{PopIII} for MH1 and MH2 are similar, within a factor of three. Unless the subclumps merge, the hydrodynamic evolution are unaffected by the substructures because they are generally connected with the central MH through cosmological filaments by which the expansion of the H II region and SN shells is halted.

Since the approaching halo is only 63.5 and 105 pc away from MH2, we expect that EE occurs. For C13, the metallicity in the region centered at the density peak with 47.4 cm^{-3} within the Jeans radius $R_J = 30.9$ pc is $1.32 \times 10^{-7} Z_{\odot}$, much smaller than the critical metallicity. For C20, we can not observe metal particles in the neighbouring cloud with maximum density 214 cm^{-3} and Jeans radius $R_J = 10.4$ pc. Smith et al. (2015) perform simulations with a neighbouring cloud at ~ 250 pc from a Pop III star-hosting cloud with $M_{\text{halo}} = 5 \times 10^5 M_{\odot}$, $M_{\text{PopIII}} = 40 M_{\odot}$, and $E_{\text{SN}} = 1 \times 10^{51}$ erg, and report the cloud is polluted with $2 \times 10^{-5} Z_{\odot}$. This higher metallicity than we obtain may be due to the larger M_{PopIII} with larger efficiency of photoionization.

We estimate the number fraction of MHs harbouring substructures. We find $\simeq 30$ MHs which have subclumps within 250 pc among 110 cosmological samples of Hirano et al. (2014, see figure D.1 of Hirano et al. (2015b)). Although further calculations are required to see whether they merge with the central MHs before the shocked gas recollapses or not, we can see that 30% of MHs will evolve as MH2.

3.2.2 CCSNe in Massive MHs

For the massive halo (MH3; $3 \times 10^6 M_{\odot}$), the H II region can not expand prior to the CCSNe (see Figures 4 and 7) because the gas accretion is more rapid than the expansion of the H II region. The central density $n_{\text{H, cen}}^{\text{life}}$ at t_{life} just before the

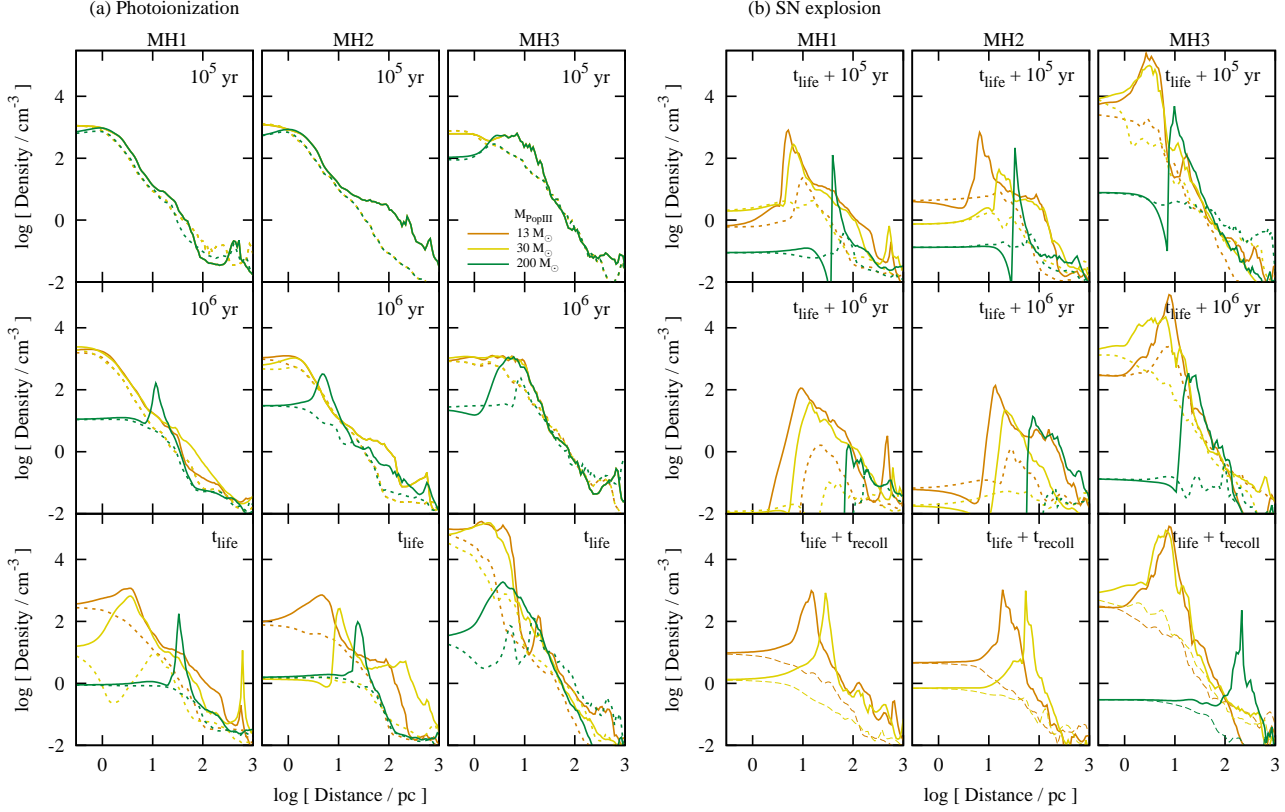


Figure 7. Gas density as a function of distance from Pop III stars with masses $M_{\text{PopIII}} = 13 M_{\odot}$ (orange curves), $20 M_{\odot}$ (yellow), and $200 M_{\odot}$ (green) hosted by minihaloes MH1 (left column), MH2 (middle), and MH3 (right). The solid and dotted curves indicate the density profile in the directions with maximum and minimum column densities at the radius of R_{halo} , respectively. The results at the time (a) 10^5 , 10^6 yr, and the lifetime t_{life} of Pop III stars during their main-sequence, and (b) 10^5 , 10^6 yr, and the time t_{recoll} when clouds collapse again after the SN explosions are shown from top to bottom row. We will show the density profiles for $M_{\text{PopIII}} = 170$ and $200 M_{\odot}$ in MH1 and MH2 at $t = t_{\text{life}} + t_{\text{recoll}}$ in Figure 11.

SNe grows up to $4.77\text{--}9.02 \times 10^5 \text{ cm}^{-3}$ (Table 3) although we turn off molecular cooling above 10^3 cm^{-3} because the gas temperature is still below the virial temperature $T_{\text{vir}} \sim 1000 \text{ K}$.

At 10^6 yr after the SN explosions, large pressure reduces the gas density in the central region, but it is not sufficient to lead the complete evacuation. While the SN ejecta barely expels in the direction of voids, blast waves are dammed and further push the gas along the filaments. The gas on the root of the filament collapses more rapid than the metal mixing, i.e., the off-central recollapse occurs as we have seen in the previous section (LH-C13 and LH-C20). Figure 4 shows that the distributions of metal particles (orange dots) remaining center with offset to the density peak. The red to green curves in Figure 8 have the steeper dependency on radius than in LH-CCSN. Consequently, the metallicity in the self-enriched region becomes $4.77 \times 10^{-7} Z_{\odot} < Z_{\text{cen}}^{\text{recol}} < 1.29 \times 10^{-5} Z_{\odot}$ and $-6.17 < [\text{Fe}/\text{H}] < -5.55$. This result implies that the next generation stars formed in this recollapsed cloud would be similar to the Pop III stars because clouds with metallicities below the critical $[\text{Fe}/\text{H}]_{\text{cr}} = -5$ will collapse in a single or several massive object(s) due to insufficient radiative cooling (Omukai 2000; Schneider et al. 2003; Chiaki et al. 2016). We revisit this issue later in Section 5.3.

3.2.3 PISN in Massive MHs

For the massive halo (MH3), the H II region can expand only $\sim 1 \text{ pc}$, albeit the copious emission of ionization photons ($Q(\text{H}) \sim 10^{50} \text{ s}^{-1}$) for PISNe. That is caused by the large accretion rate into the massive halo (see Figures 4 and 7).

At 10^6 yr after the SN explosions, large pressure leads the gas in the central region to be evacuated as for the low-mass MHs. For P170, the recollapse is delayed to 5.85 Myr because of the energetic explosion. For P200, the gas recollapses at the time 28.5 Myr after the SN.

The metallicity in the recollapsing region is $Z_{\text{cen}}^{\text{recol}} = 1.49 \times 10^{-4} Z_{\odot}$ and $9.10 \times 10^{-4} Z_{\odot}$ ($[\text{Fe}/\text{H}]_{\text{cen}}^{\text{recol}} = -3.93$ and -3.04) for P170 and P200, respectively, above the critical metallicity $[\text{Fe}/\text{H}]_{\text{cr}}$ for the cloud fragmentation so that low-mass EMP stars with the abundance ratio of PISNe which can survive until the present day are likely to be formed. Following the recommendation of Karlsson et al. (2008), we estimate the calcium abundance $[\text{Ca}/\text{H}]_{\text{cen}}^{\text{recol}} = -3.26$ and -2.25 , respectively. We also confirm that a PISN can create the highly enriched region due to its large mass of ejected metals as Karlsson et al. (2008) point out. We estimate the number fraction of MHs which will host such stars in Section 4.3.

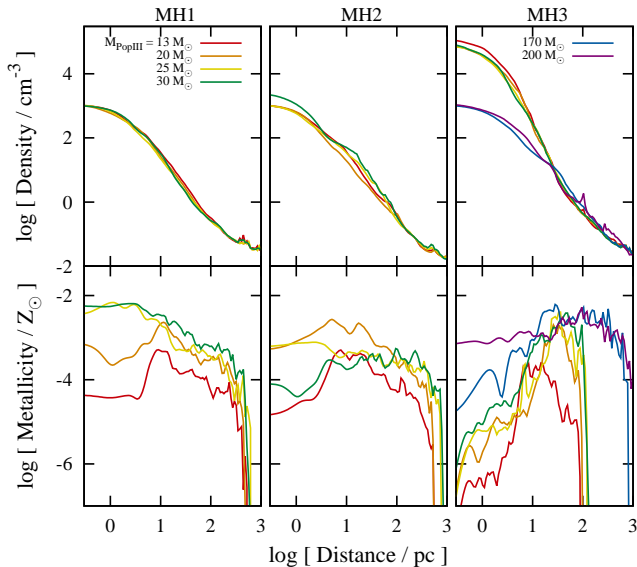


Figure 8. Gas density (top panels) and metallicity (bottom) as a function of distance from the collapse center for MH1 (left column), MH2 (middle), and MH3 (right) with progenitor masses $M_{\text{PopIII}} = 13\text{--}200 M_{\odot}$ from red to purple at the recollapsing time $t = t_{\text{life}} + t_{\text{recol}}$. We will show the results for $M_{\text{PopIII}} = 170$ and $200 M_{\odot}$ in MH1 and MH2 in Figure 11.

Table 4. Properties of externally enriched haloes

Halo	M_{PopIII} [M_{\odot}]	Cloud	D [pc]	$M_{\text{halo}}^{\text{ngb}}$ [M_{\odot}]	$R_{\text{halo}}^{\text{ngb}}$ [pc]
MH1	170	1A	281	1.73×10^7	357
		1B	909	2.72×10^6	192
		1C	393	6.05×10^6	251
		1D	656	1.77×10^6	167
		1E	648	1.01×10^6	138
		1F	903	1.54×10^6	159
		1G	593	8.22×10^6	278
	200	1A	210	2.14×10^7	392
		1B	873	3.21×10^6	208
		1C	335	1.54×10^6	351
		1D	613	2.29×10^6	186
		1E	550	1.07×10^6	144
		1F	886	2.66×10^6	195
		1H	606	1.62×10^6	165
MH2	170	MH2	—	3.03×10^6	211
		2A	643	3.14×10^6	213
		2B	613	1.85×10^6	179
		2C	1099	2.88×10^6	207
		2D	1006	7.40×10^5	132
	200	MH2	—	2.93×10^6	210
		2A	632	3.20×10^6	216
		2B	615	1.86×10^6	180
		2E	1312	7.35×10^6	285
		2F	1306	4.25×10^5	110

(4) D : distance of enriched neighbouring halo from the central MH. (5, 6) $M_{\text{halo}}^{\text{ngb}}$, $R_{\text{halo}}^{\text{ngb}}$: virial mass and radius of a neighbouring halo.

3.2.4 Summary of dependency of metallicity on M_{halo} and M_{PopIII}

As we have seen so far, the metallicity range resulting from the self-enrichment of MHs spreads a wide range from $[\text{Fe}/\text{H}]_{\text{cen}}^{\text{recol}} = -6.17$ to -2.84 , depending on M_{halo} , M_{PopIII} and the presence of substructures. In case we consider large M_{halo} and small M_{PopIII} , H II region are ‘extinguished’ by the rapid gas accretion along the filaments, and by succeeding SN explosion metal can not sufficiently penetrate into the recollapsing region at the limb of the MH connecting to the filaments as schematically shown in Figure 9 (off-central recollapse). This occurs for LH-C13 and C20, and resulting metallicity is below $[\text{Fe}/\text{H}]_{\text{cen}}^{\text{recol}} = -3$. Especially for HH-CSSN, the reduction of metallicity is remarkable to be below $[\text{Fe}/\text{H}]_{\text{cen}}^{\text{recol}} = -5$. In this metallicity range, no CN-EMP stars have been observationally found so far (Figure 1). Therefore, we hereafter call this enrichment mode as the ‘ineffective IE’ mode as a subset of the cases with the off-central recollapse. We will estimate the condition for the mode in Section 4.2.

A series of earlier works reports that the recollapsing regions formed through IE have above the critical metallicity (Ritter et al. 2012, 2015, 2016; Sluder et al. 2016). They however consider that $Q(\text{H}) = 6 \times 10^{49} \text{ s}^{-1}$, corresponding to $M_{\text{PopIII}} = 60 M_{\odot}$ (Schaerer 2002) and $M_{\text{halo}}^{\text{col}} = 1 \times 10^6 M_{\odot}$, where H II region sufficiently break the Pop III hosting cloud in MHs. By performing simulations with lower M_{PopIII} and higher M_{halo} , we find the ineffective IE mode.

3.3 External enrichment

PISN in Low-mass MHs

In the case of LH-PISN, Figures 2 and 3 show that H II region expands beyond the virial radius (~ 100 pc), since the halo mass is less than the critical mass. Ionizing photons expel to the void regions, but the gas temperature does not change along the filaments of the cosmic web, which leads the shape of H II region to be bipolar. The gas density decreases down to $\sim 1 \text{ cm}^{-3}$ due to strong pressure as shown by red and green curves in Figure 7, which is consistent with the one-dimensional calculations of Kitayama et al. (2004) and Whalen et al. (2008).

Figure 10 shows the projection of density for LH-PISN. Since the SN shocks go through the rarefied regions, the enriched region extends to $\sim 1\text{--}1.5$ kpc from the locus of the progenitors at $\simeq 50$ Myr after the SN. At that time, the gas density does not reach 10^3 cm^{-3} in the halo hosting the progenitors. Before the self-enrichment, the central density of some neighbouring haloes (dubbed ‘1A’ and ‘2E’) exceeds $\sim 10^5 \text{ cm}^{-3}$ by the halo mergers although we do not consider molecular cooling at that regions. We terminate the simulation at $\simeq 50$ Myr after the SN explosions because the computational timestep becomes shorter and because star formation activity would begin in the neighbouring haloes.

Within 1.5 kpc from the central halo, several neighbouring haloes reside. To study whether the neighbouring haloes are enriched or not, we pick up the ones with non-zero metallicities within the virial radii. The properties of haloes are listed in Table 4, and their loci are shown in Figure 10. The configurations of these haloes are different

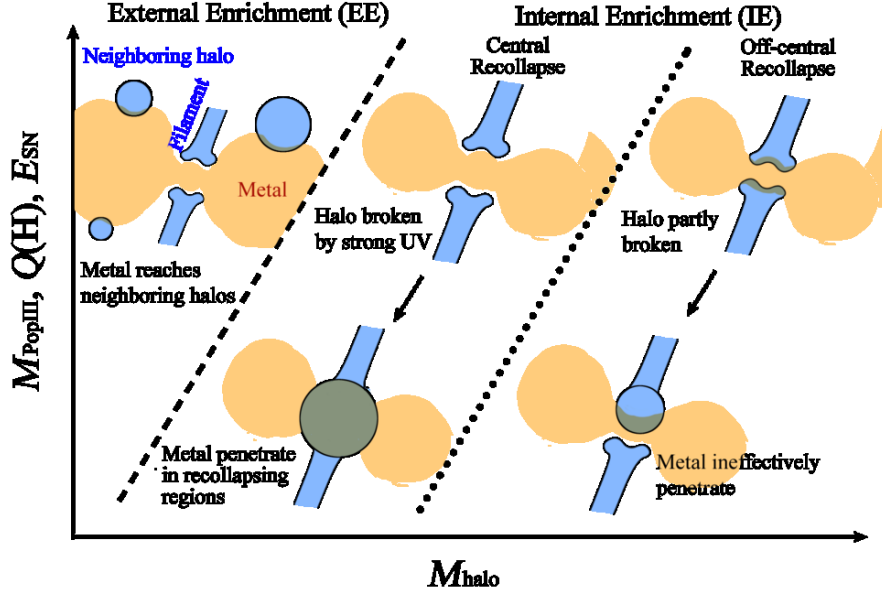


Figure 9. Schematic picture of the different modes: enrichment processes of a cloud which collapse after the SN explosion of a Pop III star. With increasing M_{PopIII} and decreasing M_{halo} , metal (orange coloured region) is dispersed in the neighbouring haloes (blue circles) because the explosion energy overcomes the halo’s binding energy (External Enrichment: EE). Otherwise, gas falls back to the central halo having hosted the Pop III star along the filamentary cosmic large-scale structure (Internal Enrichment: IE). Normally, the gas recollapses to the halo center with metals (central recollapse). For decreasing M_{PopIII} and increasing M_{halo} , the region compressed by shock in the direction of filaments collapse more rapidly than it falls back into the center, and acquires metals inefficiently (off-central recollapse).

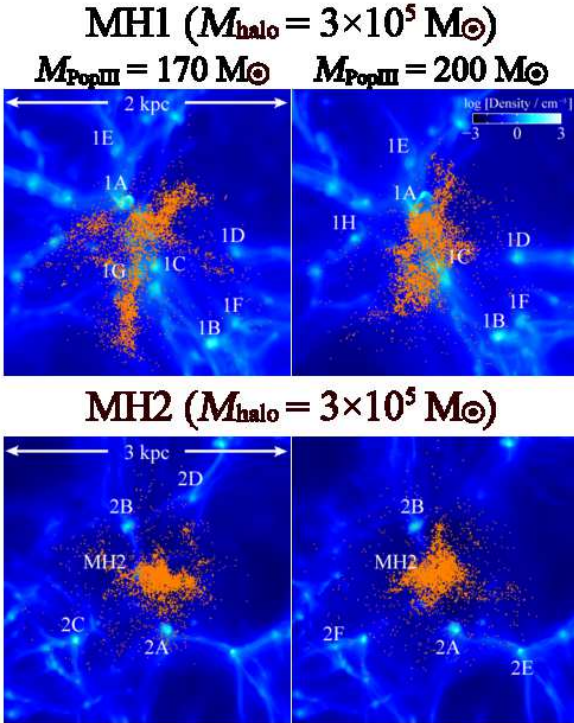


Figure 10. Density projection for PISNe with progenitor masses of $M_{\text{PopIII}} = 170$ and $200 M_{\odot}$ in low-mass haloes (MH1 and MH2) at ≈ 50 Myr after SNe. Labels show the halo having hosted the Pop III star and neighbouring haloes within whose virial radius the average metallicity is non-zero.

between for P170 and P200 because t_{life} and elapse time after SNe are different. The bottom panels of Figure 11 show the metallicity profile. In most cases, the gas with metals is dammed at the regions with density $\gtrsim 10 \text{ cm}^{-3}$ and does not reach the central densest region of the neighbouring haloes as Chen et al. (2017) reported. Only MH1-P170, metals are penetrated into the center of a neighbouring halo 1A, which is formed through mergers of some haloes. By the merger of one of the progenitors which has been superficially polluted, the metals are incorporated into the central region. Still, the average metallicity within the Jeans radius of 2.4 pc is $6.4 \times 10^{-6} Z_{\odot}$, which is below the critical metallicity $[\text{Fe}/\text{H}]_{\text{cr}}$, and low-mass stars are unlikely to be formed.

4 CRITICAL HALO MASSES

4.1 Boundary between IE and EE

In this section, we quantitatively define the boundary between IE and EE which is schematically shown by dashed line in Figure 9. First of all, the critical halo mass below which EE realises is defined so that the explosion energy E_{SN} , including the effect of radiative loss, is sufficiently above the gas binding energy $E_{\text{bin}} = GM_{\text{halo}}M_{\text{pri}}/R_{\text{halo}}$. We then introduce the ratio $C = E_{\text{SN}}/E_{\text{bin}}$. When the H II region fails to expand, $C > C_{\text{cr}} = 300$ is required for the MH to be brown away by the explosion, as confirmed by one-dimensional calculations of Kitayama & Yoshida (2005). On the other hand, when H II region expands, since the SN shocks go through the rarefied gas, $C_{\text{cr}} = 1$ is applied. We then estimate the critical halo mass below which the ratio

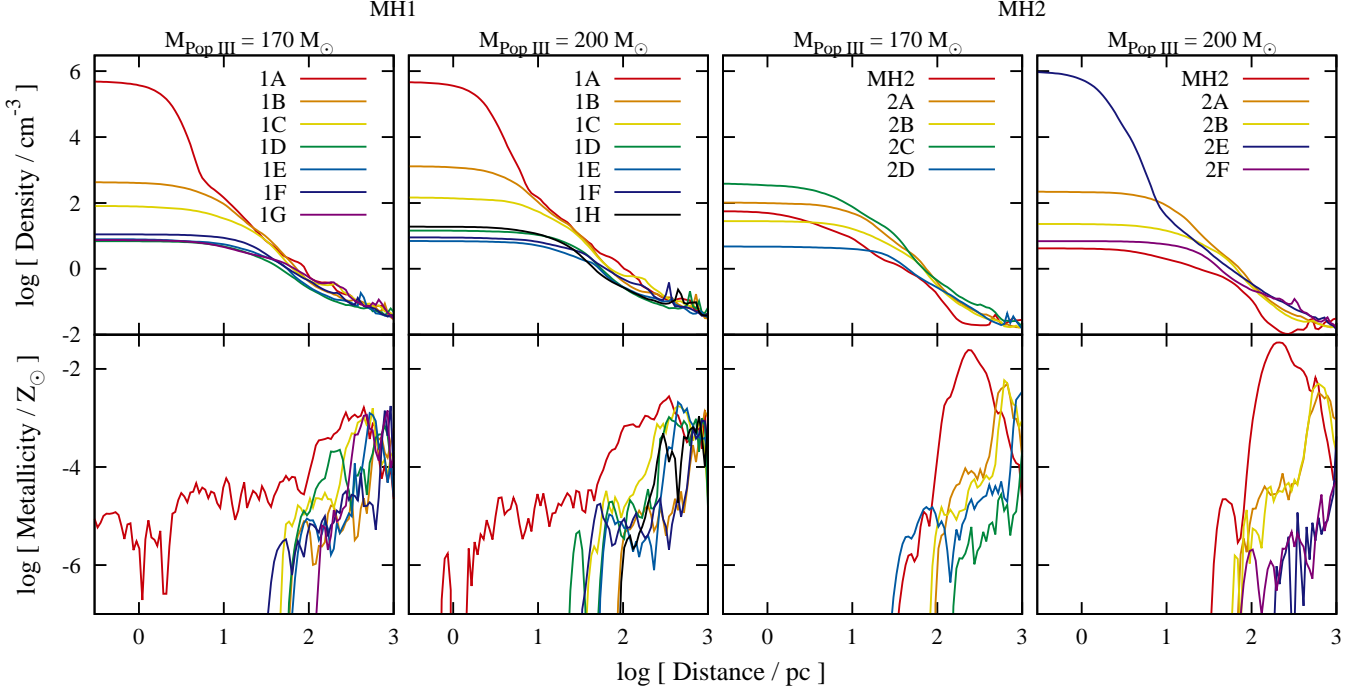


Figure 11. Density (top) and metallicity (bottom) distributions as a function of distance from the center of the halo having hosted the Pop III star and the enriched neighbouring haloes for PISNe in low-mass haloes (MH1 and MH2). The labels of haloes are the same as the ones indicated in Figure 10 for each halo and $M_{\text{Pop III}}$.

exceeds C_{cr} as,

$$M_{\text{halo,cr}}^{\text{blow}} = 4.07 \times 10^6 M_{\odot} C_{\text{cr}}^{-3/5} \left(\frac{E_{\text{SN}}}{1.0 \times 10^{51} \text{ erg}} \right)^{3/5}, \quad (6)$$

at $z_{\text{recol}} \simeq 20$ with matter to baryon mass ratio 6.

Whether the gas has been diluted by the preceding photoionization is described as the critical halo mass above which the Strömberg radius fails to exceed the radius $r_{\text{D}} = v_{\text{D}} t_{\text{life}}$ of a D-type ionization front (I-front) within t_{life} to expand as an R-type front:

$$M_{\text{halo,cr}}^{\text{ion}} = 2.5 \times 10^6 M_{\odot} \left(\frac{v_{\text{D}}}{20 \text{ km s}^{-1}} \right)^{3/4} \times \left(\frac{t_{\text{life}}}{5 \text{ Myr}} \right)^{3/4} \left(\frac{Q(\text{H})}{10^{49} \text{ s}^{-1}} \right)^{3/4} \left(\frac{1+z_{\text{col}}}{20} \right)^{-3/2} \quad (7)$$

for the initial radial profile of clouds $\propto r^{-2}$, where v_{D} is the velocity of the D-type I-front (Kitayama et al. 2004). In Figure 12, the dashed curve shows $M_{\text{halo,cr}}^{\text{ion}}$ with t_{life} and $Q(\text{H})$ of the results of Schaerer (2002).

Then, the condition for EE is written as

$$M_{\text{halo}} < \begin{cases} M_{\text{halo,cr}}^{\text{blow}}(C_{\text{cr}} = 1) & \text{for } M_{\text{halo}} < M_{\text{halo,cr}}^{\text{ion}} \\ M_{\text{halo,cr}}^{\text{blow}}(C_{\text{cr}} = 300) & \text{for } M_{\text{halo}} > M_{\text{halo,cr}}^{\text{ion}} \end{cases} \quad (8)$$

When H II region can expand ($M_{\text{halo}} < M_{\text{halo,cr}}^{\text{ion}}$; top-left of Figure 12), MHs with $M_{\text{halo}} < M_{\text{halo,cr}}^{\text{blow}}(C_{\text{cr}} = 1) = 4.07 \times 10^6 M_{\odot}$ (CCSN) and $2.74 \times 10^7 M_{\odot}$ (PISN), that is, the all regions with $M_{\text{halo}} < M_{\text{halo,cr}}^{\text{ion}}$ undergo EE. When H II region fails to expand ($M_{\text{halo}} > M_{\text{halo,cr}}^{\text{ion}}$), MHs with $M_{\text{halo}} < 1.33 \times 10^5 M_{\odot}$ (CCSN) and $8.94 \times 10^5 M_{\odot}$ (PISN) undergo EE. Although a tiny fraction of the region with $M_{\text{halo}} < M_{\text{halo,cr}}^{\text{ion}}$ is favoured for EE for CCSN, let us define the condition for

EE is $M_{\text{halo}} < M_{\text{halo,cr}}^{\text{ion}}$ for simplification. For convenience, we present the fitting formula of the boundary as

$$M_{\text{halo,cr}}^{\text{ion}} \simeq 6 \times 10^5 M_{\odot} \times \left\{ \left(\frac{M_{\text{Pop III}}}{25 M_{\odot}} \right) \left[1 - \exp \left(-\frac{M_{\text{Pop III}}}{25 M_{\odot}} \right) \right] \right\}^{3/4} \quad (9)$$

valid for $M_{\text{Pop III}} = 10\text{--}200 M_{\odot}$ and $z_{\text{col}} = 20\text{--}30$.

Note that MH1-C30 and MH2-C30 are marginally judged to be the models with EE by this criterion. The estimation of the critical halo mass is still simplified. More simulations with various initial parameters can make the estimation more accurate.

In Figure 12, we also plot the results of previous works. Their results agree with our criterion. Smith et al. (2015) find that EE occurs with the initial halo mass $M_{\text{halo}} = 5 \times 10^5 M_{\odot}$ and $M_{\text{Pop III}} = 40 M_{\odot}$, and $Z_{\text{cen}} = 2 \times 10^{-5} Z_{\odot}$. Ritter et al. (2016) show that IE occurs with $M_{\text{halo}} = 1 \times 10^6 M_{\odot}$ and $M_{\text{Pop III}} = 60 M_{\odot}$, and resulting metallicity is $2\text{--}5 \times 10^{-4} Z_{\odot}$. To consider the accretion of pristine gas into MHs, we plot them on M_{halo} 1.2 times larger than their initial values. These parameters are slightly above and below $M_{\text{halo,cr}}^{\text{ion}}$, respectively.

4.2 Condition for ineffective IE

We also define the condition for the ineffective IE presented in Section 3.2.4. In Figure 9, the region of ineffective IE exists lower right corner, where a less massive Pop III star explodes in a massive minihalo. As the necessary condition for this mode, SN remnants should undergo off-central recollapse, where H II region can hardly break the Pop III star-forming clouds, and even continue to collapse with ineffec-

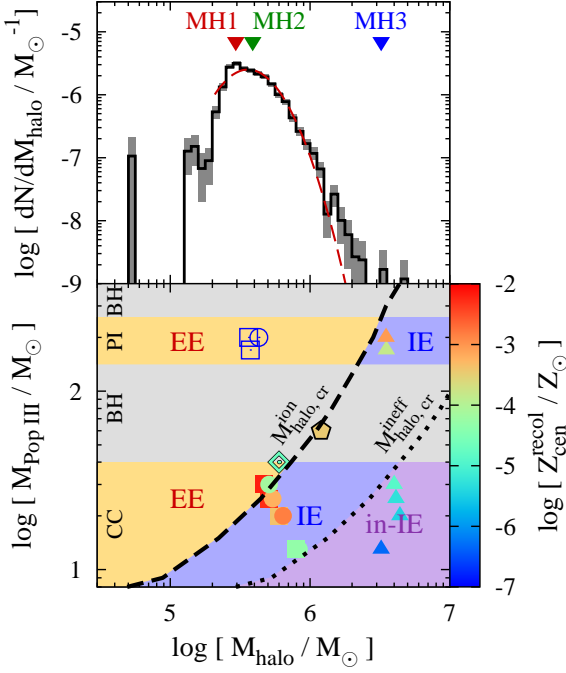


Figure 12. **Top:** Mass distribution of minihaloes obtained by cosmological simulations by Hirano et al. (2015a) with Poisson errors (black solid curve). It is fitted by a log-normal function with the mean $\mu = 12.96$ and standard deviation $\sigma = 0.41$ (red dashed curve). The triangles indicate $M_{\text{halo}}^{\text{col}}$ of MH1, MH2, and MH3. **Bottom:** Regions on the $M_{\text{PopIII}}-M_{\text{halo}}$ plane coloured by yellow, blue, and purple indicate the parameter spaces where the external enrichment (EE), internal enrichment (IE), and ineffective IE (in-IE; see Section 4.3) are realized, respectively. The enrichment occurs in the range of M_{PopIII} exploding as CCSNe (indicated by ‘CC’) and PISNe (‘PI’) while not in the grey-coloured region with a label ‘BH’ (Heger & Woosley 2002). The squares, circles, and triangles indicate M_{PopIII} and $M_{\text{halo}}^{\text{recol}}$ in MH1, MH2, and MH3, respectively. We also plot the results of Smith et al. (2015, diamond) and Ritter et al. (2016, pentagon). The filled symbols indicate the models with IE, and are color-coded according to the metallicity in the recollapsing regions. The open symbols indicate the models with EE. The thin and thick dotted curves represent the critical halo masses $M_{\text{halo,cr}}^{\text{ion}}$ (equation 7) and $M_{\text{halo,cr}}^{\text{ineff}}$ (equation 10).

tively accreting metals. The critical condition (dashed curve in Figure 12) is consistent with the boundary between the central recollapse and off-central recollapse seen in our simulations. The parameters (M_{halo} and M_{PopIII}) for MH1–C13 and C20, where the off-central recollapse occurs, are below the dotted line. The legend’s colour shows the metallicities in the recollapsing regions in the simulations. The boundary separates the parameters which gives the metallicities above and below $[\text{Fe}/\text{H}]_{\text{cen}}^{\text{recol}} \sim -3$. We define the ineffective IE as the cases with $[\text{Fe}/\text{H}]_{\text{cen}}^{\text{recol}} \leq -5$. For smaller metallicity boundary, larger M_{halo} is permitted because it can retain more dense pristine clouds during MS of Pop III stars into which metals more hardly penetrate. Multiplying $M_{\text{halo,cr}}^{\text{ion}}$ with a factor of six can reproduce the critical halo mass $M_{\text{halo,cr}}^{\text{ineff}}$ above which ineffective IE occurs as indicated by

Table 5. Fractions of minihaloes for each enrichment process

SN	Enr. mode	$[\text{Fe}/\text{H}]_{\text{cen}}^{\text{recol}}$	Fraction	
			flat IMF	Salpeter IMF
PI	EE	$< [\text{Fe}/\text{H}]_{\text{cr}}$	$\simeq 1$	$\simeq 1$
	IE	$> [\text{Fe}/\text{H}]_{\text{cr}}$	4.60×10^{-6}	7.23×10^{-6}
CC	EE	$< [\text{Fe}/\text{H}]_{\text{cr}}$	0.423	0.127
	IE	$> [\text{Fe}/\text{H}]_{\text{cr}}$	0.566	0.824
	in-IE	$< [\text{Fe}/\text{H}]_{\text{cr}}$	0.011	0.049

Note — (2) Enrichment mode: external enrichment (EE), internal enrichment (IE), and ineffective IE (in-IE). See Section 4.3 for the detailed descriptions.

the dotted curve:

$$M_{\text{halo,cr}}^{\text{ineff}} = 4 \times 10^6 M_{\odot} \times \left\{ \left(\frac{M_{\text{PopIII}}}{25 M_{\odot}} \right) \left[1 - \exp \left(-\frac{M_{\text{PopIII}}}{25 M_{\odot}} \right) \right] \right\}^{3/4} \quad (10)$$

4.3 Number fraction of MHs for each enrichment process

As a next step, we estimate the number fractions of MHs where each enrichment mode occurs. For this purpose, we use the mass distribution of 1538 MHs hosting Pop III stars taken from a cosmological simulations (Hirano et al. 2015a). The top panel of Figure 12 shows it with error bars estimated as the Poisson error. The lower limit is determined by the minimum virial temperature $T_{\text{vir}} = 1000$ K above which primordial gas can collapse by the radiative cooling owing to hydrogen molecules while the upper limit is determined by the redshift-dependent intensity of dissociation photons from the neighbouring haloes. In this range, the mass distribution of MHs is fitted by a log-normal function truncated at those masses. With the least squares, its mean and standard deviation are estimated as $\mu = 12.96 \pm 0.02$ and $\sigma = 0.41 \pm 0.02$, respectively (red dashed curve in Figure 12).

Since the critical halo masses ($M_{\text{halo,cr}}^{\text{ion}}$ and $M_{\text{halo,cr}}^{\text{ineff}}$) depend on M_{PopIII} , we should assume some IMF of Pop III stars: the flat and Salpeter IMFs with slope indices 0 and -2.35 , respectively. Using this halo mass function and Pop III IMF, the number fractions of MHs with each enrichment mode are estimated for PISNe and CCSNe (Table 5).

For PISNe, our simulations suggest that almost all MHs undergo EE in the relevant mass range by the large efficiency of photoionization and large explosion energy regardless of the Pop III IMF. This shows that negligible fractions ($\sim 10^{-6}$ – 10^{-5}) of MHs create low-mass EMP stars with the abundance ratio of PISNe even if such massive progenitors exist. It is consistent with the observations showing that such EMP stars have not been observed so far as further discussed in the next section.

For CCSNe, EE is predicted to occur 42% and 13% of MHs for the flat and Salpeter IMFs, respectively. More than half of MHs are sufficiently self-enriched to form metal-poor star-forming clouds with metallicities $[\text{Fe}/\text{H}]_{\text{cen}}^{\text{recol}} > -5$. For the flat and Salpeter IMF, only 1% and 5% of MHs more massive than $M_{\text{halo,cr}}^{\text{ineff}}$, thereby they undergo ineffective IE.

5 COMPARISON WITH THE OBSERVATIONS OF EMP STARS

5.1 Formation of massive Pop III exploding as PISNe

Although we see that IE occurs for our HH-PISN models, such a massive halo with $\geq 3 \times 10^6 M_{\odot}$ is very rare (Figure 12). This indicates that Pop II stars which inherit elemental abundance ratios of PISNe are hardly formed in the metallicity range of $[\text{Fe}/\text{H}] > -5$ because almost all MHs are blown away by the copious emission of ionizing photons from massive Pop III stars and energetic explosion of PISNe even if they exist. Although 1,401 stars with $[\text{Fe}/\text{H}] < -2.5$ have already been observed until September 2017, EMP stars with the elemental abundance ratio of PISNe have not been observed yet, or only one candidate (Aoki et al. 2014). Our results suggest that 10^5 – 10^6 stars should be observed to find a star with a sign of PISNe.

Some researches suggest that even the existence of the progenitors is unlikely. Some numerical works show the fragmentation of primordial clouds (Bromm et al. 1999) and accretion disk around a Pop III protostar (Greif et al. 2011; Stacy et al. 2012; Susa et al. 2014; Hosokawa et al. 2016; Hirano & Bromm 2017). Also, it has been suggested that even with the Salpeter IMF the inefficient sampling of stellar mass fails to create such massive stars exploding as PISNe, because MHs are expected to have smaller star formation efficiencies due to their lack of coolant (de Bannassuti et al. 2014, 2017).

5.2 C-enhanced EMP stars

We have calculated the metallicity in the recollapsing region for CCSNe which produce the C-normal abundance ratio. For stars with $[\text{Fe}/\text{H}] < -3$, the fraction of CE-EMP stars increase as $[\text{Fe}/\text{H}]$ decreases (Beers & Christlieb 2005). In order to reproduce the elemental abundance of CE-EMP stars, the model of faint SNe (FSNe) is often employed. In the mixing-fallback scenario, the inner layer of ejecta enriched with Fe-peak elements sink into central compact objects while the outer C-rich layer is ejected. Although the models of a single FSN can well reproduce abundance patterns of CE-EMP stars, it has not been numerically shown that the metallicity of the gas enriched by a FSN can reproduce the absolute metallicity, or Fe abundance $[\text{Fe}/\text{H}]$.

Our results can be applied to general SN models with the common progenitor mass M_{PopIII} and explosion energy E_{SN} , which determine the density distribution of the ambient gas. Since we do not calculate the back reaction of the metal distribution to the hydrodynamic motions of gas such as the additional radiative cooling owing to metal and dust, we can reproduce the spatial distribution of metal ejected from any SN models by just scaling the total metal mass. We here employ models tailored to reproduce the elemental abundances of CE-EMP stars, HE0557-4840 (HE0557), HE0107-5240 (HE0107), HE1327-2326 (HE1327), and SMSSJ0313-6708 (SM0313), presented by Ishigaki et al. (2014, I14), Tominaga et al. (2014, T14), and Marassi et al. (2015, M15). To compare with observations, we estimate $[\text{Fe}/\text{H}]_{\text{cen}}^{\text{recol}}$ from the iron mass $M_{\text{Fe}}^{\text{ej}}$ of each SN model with equation (5). Since the efficiency of metal dispersion varies

among the MHs, we estimate $[\text{Fe}/\text{H}]_{\text{cen}}^{\text{recol}}$ for each MH as shown in Table 6. The MH models which can reproduce $[\text{Fe}/\text{H}]_{\text{obs}}$ within 0.5 dex are written in bold.

For the star HE0557 with a moderate C-enhancement $[\text{C}/\text{Fe}] = 1.76$, the resulting metallicities for the progenitor model of I14 for MH1 is consistent with the observed metallicity $[\text{Fe}/\text{H}]_{\text{obs}} = -4.79$. The model of T14 for MH2 can explain the formation of HE0557. Note that E_{SN} in their model is 5.0×10^{51} erg while $E_{\text{SN}} = 1.0 \times 10^{51}$ erg in our simulations. Simulations with $E_{\text{SN}} = 5.0 \times 10^{51}$ erg would result in smaller metallicities because the metals would be blown away to larger distances. For M15, the metallicity $[\text{Fe}/\text{H}]_{\text{cen}}^{\text{recol}}$ is smaller than the observed abundance because of the larger mass-cut $M_{\text{cut}} = 5 M_{\odot}$ and accordingly smaller ejected metal mass. For the massive halo MH3, where ineffective IE takes place, the metallicities are smaller than the observed one by more than three orders of magnitude for every progenitor model. This indicates that IE from FSN hosted by MH1 and MH2 with normal halo mass $M_{\text{halo}} \sim 3 \times 10^5 M_{\odot}$ can explain the formation of the C-moderate star.

For the star HE0107, $M_{\text{Fe}}^{\text{ej}}$ and $[\text{Fe}/\text{H}]_{\text{cen}}^{\text{recol}}$ are consistent among the literatures. Although M15 present the progenitor model, their best-fit model is for $M_{\text{PopIII}} = 35 M_{\odot}$ with which we do not simulate the process of metal dispersion. In the models of I14 and T14 for MH1, $[\text{Fe}/\text{H}]_{\text{en}}^{\text{recol}} = -5.53$ and -5.78 , respectively, are slightly smaller than $[\text{Fe}/\text{H}]_{\text{obs}}$ by a factor of 0.1–0.3 dex.¹ The predicted metallicity for MH2 is smaller than for MH1 because a pristine cloud falls into the central halo before the shocked shell accretes again. As for HE0557, the metallicity for MH3 is further smaller than MH1 by three orders of magnitude. Let us thus conclude that IE from a FSN hosted by a less-massive halo without sub-structures is most likely to explain the formation of the star HE0107.

For HE1327, the tendency of metallicity among MHs is the same as for HE0107. However, the predicted metallicity is smaller than the observed one by a factor of at least 0.8–0.9 dex for MH1. The FSN scenario generally predicts the smaller mass of ejected metal relative to normal CCSNe due to the fallback of material into the core. To create the star-forming region simultaneously satisfying the large C-enhancement $[\text{C}/\text{Fe}] = 4.18$ and metallicity $[\text{Fe}/\text{H}] = -5.71$, multiple SN explosions including FSN would be required.

For SM0313, Keller et al. (2014) measure only the upper limit of its iron abundance. Therefore, we compare the carbon abundance predicted from our simulations with the one constrained by the observation. I14 and M15 present the progenitor models which can reproduce its elemental abundance ratio. The best-fit model by M15 is with $E_{\text{SN}} = 80 M_{\odot}$, for which we here do not calculate. The model with $M_{\text{PopIII}} = 25 M_{\odot}$ of I14 predicts the carbon mass of $M_{\text{C}}^{\text{ej}} = 0.288 M_{\odot}$. For MH1, we can predict the carbon abundance in the recollapsing clouds to be $[\text{C}/\text{H}]_{\text{cen}}^{\text{recol}} = -2.49$, which is consistent with the observation $[\text{C}/\text{H}]_{\text{obs}} = -2.6$ with a 3D-LTE model. For MH2, the C abundance is smaller

¹ Take care that the iron abundance $[\text{Fe}/\text{H}]_{\text{cen}}^{\text{recol}} < [\text{Fe}/\text{H}]_{\text{cr}}$ does not violate the critical condition for the formation of low-mass stars in the CE-EMP regime. Instead of silicate grains, carbon grains are dominant species and gives the critical C abundance as $-4.65 < [\text{C}/\text{H}]_{\text{cr}} < -3.01$ (Marassi et al. 2014).

Table 6. CEMP stars

Star	Observation		Model					This work	
	$[\text{C}/\text{Fe}]_{\text{obs}}$	$[\text{Fe}/\text{H}]_{\text{obs}}$	Ref.	M_{PopIII} [M_{\odot}]	E_{SN} [10^{51} erg]	M_{cut} [M_{\odot}]	$M_{\text{Fe}}^{\text{ej}}$ [M_{\odot}]	Halo	$[\text{Fe}/\text{H}]_{\text{cen}}^{\text{recol}}$
HE0557	1.76	−4.79	I14	25	1	1.7	2.2×10^{-3}	MH1	−4.34
								MH2	−5.29
								MH3	−7.34
			T14	25	5.0	1.78	6.80×10^{-3}	MH1	−3.85
								MH2	−4.80
								MH3	−6.85
			M15	20	1.0	5	2.82×10^{-5}	MH1	−7.16
								MH2	−6.61
								MH3	−9.24
HE0107	4.12	−5.44	I14	25	1	1.7	1.4×10^{-4}	MH1	−5.53
							MH2	−6.48	
							MH3	−8.54	
			T14	25	5.0	1.90	8.02×10^{-5}	MH1	−5.78
								MH2	−6.73
								MH3	−8.78
HE1327	4.18	−5.71	I14	25	1	1.7	1.1×10^{-5}	MH1	−6.64
							MH2	−7.59	
							MH3	−9.64	
			T14	25	0.72	1.69	1.53×10^{-5}	MH1	−6.50
								MH2	−7.45
								MH3	−9.50
			M15	30	1.6	5	1.58×10^{-5}	MH1	−6.66
								MH2	−8.63
								MH3	−9.37
	$[\text{C}/\text{Fe}]_{\text{obs}}$	$[\text{C}/\text{H}]_{\text{obs}}$					M_{C}^{ej} [M_{\odot}]		$[\text{C}/\text{H}]_{\text{cen}}^{\text{recol}}$
SM0313	> 4.9	−2.6	I14	25	1	2.0	2.88×10^{-1}	MH1	−2.49
								MH2	−3.43
								MH3	−5.48

Note — The observed data $[\text{C}/\text{Fe}]_{\text{obs}}$ and $[\text{Fe}/\text{H}]_{\text{obs}}$ for the CE-EMP stars are taken from SAGA database and references therein. Using the Fe mass $M_{\text{Fe}}^{\text{ej}}$ ejected from the progenitors modeled by Ishigaki et al. (2014, I14), Tominaga et al. (2014, T14), and Marassi et al. (2015, M15), we estimate the iron abundance $[\text{Fe}/\text{H}]_{\text{en}}^{\text{recol}}$ in the recollapsing region when each progenitor explodes in MH1, MH2, and MH3. The MH models in which $[\text{Fe}/\text{H}]_{\text{en}}^{\text{recol}}$ is close to $[\text{Fe}/\text{H}]_{\text{obs}}$ within 0.5 dex are written in bold.

as $[\text{C}/\text{H}]_{\text{cen}}^{\text{recol}} = -3.43$ because the pristine clouds merge with the central cloud. It is likely that IE from a single FSN hosted by isolated less-massive halo can explain the formation of the most iron-poor star observed.

5.3 Critical metallicity

For HH-CCSN, the metallicity resulting from the off-central recollapse is very small, less than $[\text{Fe}/\text{H}] < -5$ (the triangle symbols in Figure 1). For FSNe exploding in MH3, the carbon fraction becomes $[\text{C}/\text{H}] < -3$ (Table 6). Figure 1 shows that EMP stars with this metallicity range ($10^{[\text{C}/\text{H}]-2.30} + 10^{[\text{Fe}/\text{H}]} < 10^{-5.07}$) have so far not been found (gray shaded region). From the theoretical point of view, clouds in such a metallicity range collapse to form a single massive objects due to the lack of cooling efficiency of dust grains (Omukai 2000; Schneider et al. 2003; Chiaki et al. 2017). On the other hand, some researchers report that the fragmentation of the accretion disk around a

Pop III protostellar core leads to low-mass star formation below the critical metallicity. Consequently, the clouds with $[\text{Fe}/\text{H}] < -5$ might have similar properties of fragmentation process, since its thermal evolution is almost identical to the primordial one.

By EE and ineffective IE modes, metallicities in the recollapsing regions do not reach the critical metallicity. Our simulations predict the number fraction of MHs which undergo EE and ineffective IE as 18–43% for CCSNe (Section 4.3). Suppose that the slightly enriched clouds in these MHs collapse to low-mass objects through the fragmentation, then the number fraction of EMP star would also become 18–43% for the simple estimation. From the number of EMP stars ever observed (1,401), the number of stars below the critical metallicity would be 252–602, which can not explain the current observations. Therefore, the scenario of dust-driven fragmentation would be favored to the current observation. We should note that the estimation may be oversimplified because we assume that the IMF of Pop

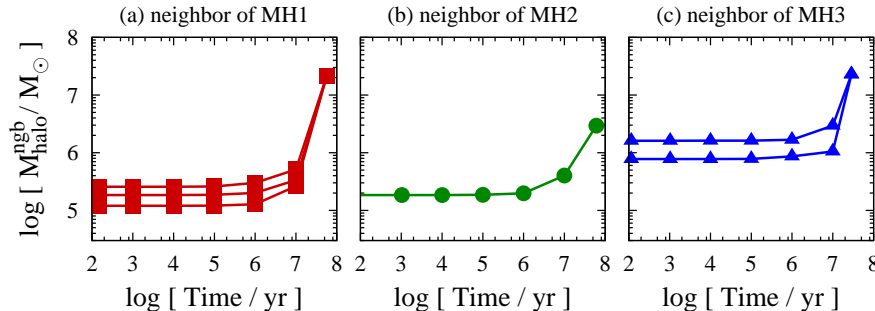


Figure 13. Mass of neighbouring haloes $M_{\text{halo}}^{\text{ngb}}$ around (a) MH1, (b) MH2, and (c) MH3 as a function of time after SN explosion.

III is uniform in all mass range of MHs and that the number of fragments is uniform in all metallicity range.

6 DISCUSSION

6.1 Enrichment efficiency of MHs

Although we have so far estimated the averaged metallicities of the recollapsing gas clouds within their Jeans length and of EMP stars which collapse earliest, the succeeding EMP star formation will take place in the whole region of MHs. We in this section estimate the average metallicity and the efficiency of metal enrichment of each MH as indicated by the dashed lines in Figure 6 and the last column of Table 3.

We introduce the mass ratio of metal and primordial gas particles within the virial radius at t_{recol} to the initial as

$$f_{\text{halo}}^{\text{met}} = \frac{M_{\text{met,halo}}^{\text{recol}}}{M_{\text{met}}^{\text{ej}}}, \quad (11)$$

$$f_{\text{halo}}^{\text{pri}} = \frac{M_{\text{pri,halo}}^{\text{recol}}}{M_{\text{pri}}^{\text{col}}}. \quad (12)$$

We only consider metal and gas particles trapped by the DM potential well with the radial velocity v_{rad} smaller than the escape velocity $v_{\text{esc}} = (2GM_{\text{halo}}/R_{\text{halo}})^{1/2}$. These factors are shown in the seventh to eighth columns of Table 3.

The simple estimation of the metallicity in a MH is the mass ratio $M_{\text{met,halo}}^{\text{recol}}/M_{\text{pri,halo}}^{\text{recol}}$. The factor $f_{\text{halo}}^{\text{met}}/f_{\text{halo}}^{\text{pri}}$ gives the correction for it. For example, $M_{\text{met,halo}}^{\text{recol}}/M_{\text{pri,halo}}^{\text{recol}} = 9.18 \times 10^{-3} Z_{\odot}$ for MH1-C30, but the 60.2% of metal is dispersed into the voids and the MH accretes the primordial gas with 2.62 times its initial mass. The dilution of metal by the factor of $f_{\text{halo}}^{\text{met}}/f_{\text{halo}}^{\text{pri}} = 0.152$ results in the eventual metallicity $1.39 \times 10^{-3} Z_{\odot}$.

CCSNe in low-mass MHs

For LH-CCSN, the metallicity range is $\sim 10^{-5}$ – $10^{-3} Z_{\odot}$, comparable to $Z_{\text{cen}}^{\text{recol}}$ in the center of the recollapsing regions. The dashed lines in Figure 6 shows that the dependency of the metallicity on M_{PopIII} is mitigated relative to the solid lines by averaging the metallicity in the wider region beyond the offset between the metal and primordial gas distributions for ineffective IE. Since the accretion of primordial gas overcomes its evacuation by SN explosion, the primordial gas mass increases by a factor of

44.2–117.2. Whereas, about a half (0.254–0.701) of metals remain in the virial radius. Consequently, the resulting metallicity is smaller than the simple estimation by a factor of $f_{\text{halo}}^{\text{met}}/f_{\text{halo}}^{\text{pri}} \sim 0.1$. For MH2-CCSN, $f_{\text{halo}}^{\text{pri}}$ is larger than for MH1-CCSN because of the halo merger.

CCSNe in massive MHs

For HH-CCSN, since a large fraction of metal does not enter the central clouds but remains within the virial radius (Figure 8), the metallicity range is 3.63×10^{-5} – $2.43 \times 10^{-4} Z_{\odot}$, slightly above the critical metallicity (Figure 6). Both $f_{\text{halo}}^{\text{met}}$ and $f_{\text{halo}}^{\text{pri}}$ are larger than those for LH-CCSN by the larger accretion rate and by the smaller t_{recol} .

PISNe in massive MHs

For HH-PISN, both $f_{\text{halo}}^{\text{met}}$ and $f_{\text{halo}}^{\text{pri}}$ is comparable those for HH-CCSN. However, the mass $M_{\text{met}}^{\text{ej}}$ is larger by a factor of ten (Table 2), the metallicity is also larger by the same factor. For MH3-P200, the metallicity is smaller than P170 because a neighbouring halo is merged, and the dense primordial envelope spreads around the enriched cloud.

6.2 Caveats

Our method can uncover the various nature of metal enrichment occurring in the transition from first-generation metal-free Pop III stars to Pop II star formation. Some caveats still remain in our methodology.

6.2.1 Star formation in neighbouring haloes

In our simulations, gas contraction is prohibited by switching off molecular cooling in the other haloes than the central one only whose stellar feedbacks interests us in this work. In reality, feedbacks from stars formed in neighbouring haloes can affect the propagation of shocks from the central star. Also, in some recollapsing regions, the metallicity will be the sum of the contributions from more than one halo, and the elemental abundance ratio will be the superposition of them. In this section we discuss the efficiency of the feedback from stars hosted by the neighbouring haloes, following the

evolution of their mass $M_{\text{halo}}^{\text{ngb}}$ in the case of P200, where we can follow the longest growth history of haloes.

The halo 1A (see Figure 10) becomes the closest to MH1. It is formed through the merger of three haloes and accretion of the intergalactic gas. Figure 13(a) shows the temporal evolution of the masses of the progenitors and 1A. The progenitors contain 1.20 , 1.84 , and $2.57 \times 10^5 M_{\odot}$ within ~ 1 Myr after the SN explosion in MH1, and they increase by a factor of two at 10 Myr. They reside at the distance $D \simeq 400$ pc from MH1. At $\simeq 50$ Myr, eventually, the mass and distance of 1A becomes $2.14 \times 10^7 M_{\odot}$ and $\simeq 200$ pc, respectively. For CCSNe, since the SN shocks should go beyond the dense filament to reach MH1, they are unlikely to affect the hydrodynamic evolution of shocks from MH1. For PISNe, although the shocks and metal will reach MH1, metal can not penetrate the central clouds as we have seen above. Since the mass evolution of the neighbouring halo of MH2 is similar to that of MH1 (Figure 13b), we can conclude that the external explosion around MH2 neither likely affect the propagation of shock and metal from MH2.

For massive halo (MH3), the neighbouring haloes are also massive with 7.76×10^5 and $1.61 \times 10^6 M_{\odot}$ in the initial state. Thus, the feedbacks from the stars in these haloes can not affect the hydrodynamics of the shocks from MH3 through the filaments connecting them to MH3. However, these haloes eventually merge with MH3 at $\simeq 10^7$ Myr after the SN. When the stars in the neighbouring haloes explode in the vicinity of MH3, the shock will affect and metal is mixed in the recollapsing region. We will examine this by permitting star formation in all haloes in forthcoming papers.

6.2.2 Multiple star formation in a halo

We assume that each MH hosts a single Pop III star. However, the number of Pop III stars which are hosted by a MH is still uncertain. Multiple star formation in a MH through the fragmentation of accretion disk around the primary protostar has been reported by some numerical works (Bromm et al. 1999; Clark et al. 2011; Greif et al. 2011; Stacy et al. 2012; Susa 2013; Susa et al. 2014; Hosokawa et al. 2016; Hirano & Bromm 2017). Majority of those fragments seem to fall in the range of CCSN. On the other hand, the explosion energy of PISNe is larger than that of CCSNe by a factor of ~ 30 . Hence if the number of fragments is $\gtrsim 30$, the total explosion energy becomes larger than that of a single PISN.

However, it has been reported that the number of fragments less than 30 thereby the multiple CCSNe would be less energetic than the PISN case investigated in the present simulations. Thus the dynamics of the ejecta of the multiple CCSNe would be in between the CCSN and PISN cases shown in the present paper. It also will increase the amount of metals by some factors. These issues will be addressed in the forthcoming papers.

6.2.3 Resolution

Metals mix into the pristine gas mainly due to the turbulence driven by fluid instabilities around shocks. Since the size of eddies cascades into smaller scales, it is ideally required to resolve down to the scale at which the eddies are

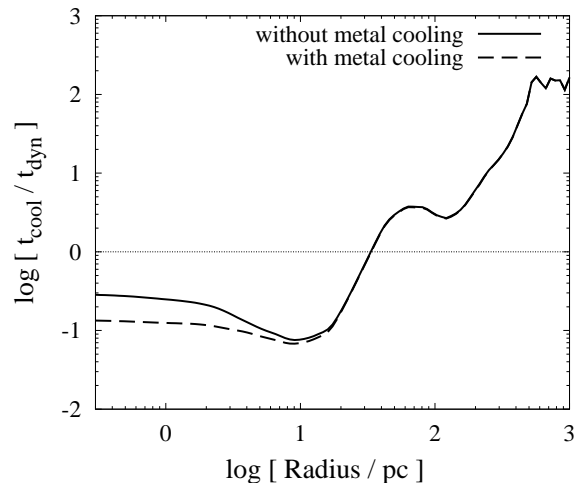


Figure 14. Ratio of cooling time t_{cool} to dynamical time-scale t_{dyn} as a function of the distance from the most dense point in the recollapsing region with a Pop III mass $M_{\text{PopIII}} = 30 M_{\odot}$ hosted by MH1. The solid curve shows the result only with cooling by primordial species, which is used in our simulations. The dashed curve shows the result by adding the contribution of metal species to gas cooling as a post-process. Here, we estimate the local free-fall time as t_{dyn} .

dissipated to see the full mixing processes. In our simulations, the minimum spacial resolution is 1.3 pc (equation 1) because of the large simulation region. In order to investigate the wide range of the parameters, we can not perform convergence tests.

Instead, we compare our results with the recent work (Chen et al. 2017): high-resolution two-dimensional simulations of the region where a SN shock hits a neighbouring pristine cloud with the minimum resolution of 0.015 pc. The separation of the target cloud and SN is 250 pc both in their work and in our LH-PISN models (Table 4). They show that SN shocks drive the Rayleigh-Taylor (RT) instability at the wall of the target cloud, but metals fails to incorporate into the clouds in most cases. The penetration of metals halt at the position 30 pc away from the cloud center (figure 9 in their paper) as seen also in our results (Figure 11). Even with our spatial resolution coarser, the behavior of metal mixing is consistent with their results.

The resolution also affects the cooling efficiency by metals in a dense snowplough shell and recollapsing region. We ignore metal cooling in the enriched gas. In the simulations of cosmological star formation history by Schaye et al. (2010), the global star formation rate is underestimated in the run without metal cooling. Ritter et al. (2016) shows that fragments insufficiently enriched by a SN undergo loitering for 10 Myr while cooling time in a clump with $\gtrsim 10^{-3} Z_{\odot}$ becomes smaller than the dynamical time-scale due to C and O fine-structure coolings to start run-away collapse. Figure 14 shows the ratio of cooling time t_{cool} to dynamical time t_{dyn} as a function of distance from the collapse center in our simulation with MH1-C30, where the metallicity in the recollapsing center becomes $6.62 \times 10^{-3} Z_{\odot}$. The ratio becomes smaller for the case with metal cooling (dashed curve) than only with contribution of primordial species (solid curve) by a factor of two. In that case, cloud

collapse becomes faster, and efficiency of metal mixing would become lower. We will confirm this in the forthcoming paper.

7 CONCLUSION

By the numerical simulations for the ionization and SN feedbacks, we estimate the metallicities in the recollapsing region which will be Pop II star-forming clouds or continue to be in the Pop III star formation regime. Thanks to the simulations with a range of initial parameters, M_{halo} and M_{PopIII} , and the initial gas distributions with various substructures, we find that a few enrichment modes can occur, and the metallicity range accordingly varies. We have found that

- there are two general enrichment processes by Pop III SNe: internal enrichment (IE) and external enrichment (EE). They exclusively occurs depending on M_{halo} and M_{PopIII} (E_{SN}).
- for CCSNe, a non-negligible fraction (13–42%) of MHs undergo EE to form recollapsing clouds with $[\text{Fe}/\text{H}]_{\text{cen}}^{\text{recol}} < -5$. So far no CN-EMP stars with the metallicity range are observed, indicating that the inefficient dust cooling prevents low-mass stars from being formed.
- for PISNe, IE takes place for a negligible fraction of MHs, which is consistent with the current observations: no EMP stars have so far been observed.
- faint supernova (FSN) models, that reproduce the abundance ratio of CE-EMP stars, can also successfully account for the absolute iron/carbon abundance of those stars in the recollapsing regions.
- we can therefore conclude that the enrichment mode IE of MHs from a single CCSN or FSN event can explain the formation of CN- and CE-EMP stars.

These findings are compared with the observations of EMP stars in the halo region of our Galaxy, and ultra-faint dwarfs (UFDs). Although our knowledge is now limited to a single event of transition from Pop III star formation to the succeeding generation of stars, i.e., the very first step of the matter cycle in ISM, we will extend this study to the early-generations of galaxies in which a number of cycles take place and directly observed by the next-decade instruments such as *JWST* and TMT.

ACKNOWLEDGMENTS

We are grateful for the anonymous referee to the suggestions and comments for our work. We also thank T. Nozawa and M. Ishigaki who kindly give us the SN models. Thanks to the deep insight of R. Schneider, L. Graziani, N. Tominaga, and T. Ishiyama, we can improve our manuscript. GC and SH are supported by Research Fellowships of the Japan Society for the Promotion of Science (JSPS) for Young Scientists. HS acknowledges the financial supports from JSPS Grant-in-Aid for Scientific Research (17H01101,17H02869,17H06360). The numerical simulations in this work are carried out on Cray XC30 at Center for Computational Astrophysics, National Astronomical Observatory of Japan and on Cray XC40 at the Yukawa Institute Computer Facility.

REFERENCES

- Abel, T., Bryan, G. L., & Norman, M. L. 2002, *Science*, 295, 93
- Aoki, W., Beers, T. C., Christlieb, N., et al. 2007, *ApJ*, 655, 492
- Aoki, W., Tominaga, N., Beers, T. C., Honda, S., & Lee, Y. S. 2014, *Science*, 345, 912
- Asplund, M., Grevesse, N., Sauval, A. J., & Scott, P. 2009, *ARA&A*, 47, 481
- Audouze, J., & Silk, J. 1995, *ApJ*, 451, L49
- Barrow, K. S. S., Wise, J. H., Norman, M. L., O’Shea, B. W., & Xu, H. 2017, *MNRAS*, 469, 4863
- Barrow, K. S. S., Wise, J. H., Aykutaalp, A., et al. 2017, arXiv:1709.04473
- Beers, T. C., & Christlieb, N. 2005, *ARA&A*, 43, 531
- Bromm, V., Coppi, P. S., & Larson, R. B. 1999, *ApJ*, 527, L5
- Bromm, V., & Loeb, A. 2003, *Nat*, 425, 812
- Bromm, V., & Yoshida, N. 2011, *ARA&A*, 49, 373
- Bromm, V. 2014, *Science*, 345, 868
- Cayrel, R., Depagne, E., Spite, M., et al. 2004, *A&A*, 416, 1117
- Clark, P. C., Glover, S. C. O., Smith, R. J., et al. 2011, *Science*, 331, 1040
- Chen, K.-J., Whalen, D. J., Wollenberg, K. M. J., Glover, S. C. O., & Klessen, R. S. 2017, *ApJ*, 844, 111
- Chen, K.-J., Heger, A., Whalen, D. J., et al. 2017, *MNRAS*, 467, 4731
- Chiaki, G., Yoshida, N., & Kitayama, T. 2013, *ApJ*, 762, 50
- Chiaki, G., Marassi, S., Nozawa, T., et al. 2015, *MNRAS*, 446, 2659
- Chiaki, G., & Yoshida, N. 2015, *MNRAS*, 451, 3955
- Chiaki, G., Yoshida, N., & Hirano, S. 2016, *MNRAS*, 463, 2781
- Chiaki, G., Tominaga, N., & Nozawa, T. 2017, *MNRAS*, 472, L115
- de Bressan, M., Schneider, R., Valiante, R., & Salvadori, S. 2014, *MNRAS*, 445, 3039
- de Bressan, M., Salvadori, S., Schneider, R., Valiante, R., & Omukai, K. 2017, *MNRAS*, 465, 926
- Dehnen, W., & Aly, H. 2012, *MNRAS*, 425, 1068
- Draine, B. T., & Bertoldi, F. 1996, *ApJ*, 468, 269
- Frebel, A., Aoki, W., Christlieb, N., et al. 2005, *Nat*, 434, 871
- Greif, T. H., Springel, V., White, S. D. M., et al. 2011, *ApJ*, 737, 75
- Hahn, O., & Abel, T. 2011, *MNRAS*, 415, 2101
- Heger, A., & Woosley, S. E. 2002, *ApJ*, 567, 532
- Hirano, S., Hosokawa, T., Yoshida, N., et al. 2014, *ApJ*, 781, 60
- Hirano, S., Hosokawa, T., Yoshida, N., Omukai, K., & Yorke, H. W. 2015, *MNRAS*, 448, 568
- Hirano, S. 2015, Ph.D. Thesis, The University of Tokyo
- Hirano, S., & Bromm, V. 2017, *MNRAS*, 470, 898
- Hosokawa, T., Hirano, S., Kuiper, R., et al. 2016, *ApJ*, 824, 119
- Ishigaki, M. N., Tominaga, N., Kobayashi, C., & Nomoto, K. 2014, *ApJ*, 792, L32
- Jappsen, A.-K., Glover, S. C. O., Klessen, R. S., & Mac Low, M.-M. 2007, *ApJ*, 660, 1332

- Karlsson, T., Johnson, J. L., & Bromm, V. 2008, *ApJ*, 679, 6-16
- Keller, S. C., Bessell, M. S., Frebel, A., et al. 2014, *Nature*, 506, 463
- Kitayama, T., Yoshida, N., Susa, H., & Umemura, M. 2004, *ApJ*, 613, 631
- Kitayama, T., & Yoshida, N. 2005, *ApJ*, 630, 675
- Komiya, Y., Suda, T., & Fujimoto, M. Y. 2015, *ApJ*, 808, L47
- Magg, M., Hartwig, T., Agarwal, B., et al. 2017, *arXiv:1706.07054*
- Marassi, S., Schneider, R., Limongi, M., et al. 2015, *MNRAS*, 454, 4250
- Marassi, S., Chiaki, G., Schneider, R., et al. 2014, *ApJ*, 794, 100
- Nagakura, T., Hosokawa, T., & Omukai, K. 2009, *MNRAS*, 399, 2183
- Nozawa, T., Kozasa, T., Habe, A., et al. 2007, *ApJ*, 666, 955
- Omukai, K. 2000, *ApJ*, 534, 809
- Planck Collaboration, Ade, P. A. R., Aghanim, N., et al. 2016, *A&A*, 594, A13
- Ritter, J. S., Safrank-Shrader, C., Gnat, O., Milosavljević, M., & Bromm, V. 2012, *ApJ*, 761, 56
- Ritter, J. S., Sluder, A., Safrank-Shrader, C., Milosavljević, M., & Bromm, V. 2015, *MNRAS*, 451, 1190
- Ritter, J. S., Safrank-Shrader, C., Milosavljević, M., & Bromm, V. 2016, *MNRAS*, 463, 3354
- Ryan, S. G., Norris, J. E., & Beers, T. C. 1996, *ApJ*, 471, 254
- Schaerer, D. 2002, *A&A*, 382, 28
- Schneider, R., Ferrara, A., Salvaterra, R., Omukai, K., & Bromm, V. 2003, *Nature*, 422, 869
- Schaye, J., Dalla Vecchia, C., Booth, C. M., et al. 2010, *MNRAS*, 402, 1536
- Schneider, R., Omukai, K., Inoue, A. K., & Ferrara, A. 2006, *MNRAS*, 369, 1437
- Schneider, R., Omukai, K., Bianchi, S., & Valiante, R. 2012a, *MNRAS*, 419, 1566
- Shapiro, P. R., & Kang, H. 1987, *ApJ*, 318, 32
- Sluder, A., Ritter, J. S., Safrank-Shrader, C., Milosavljević, M., & Bromm, V. 2016, *MNRAS*, 456, 1410
- Smith, B. D., Wise, J. H., O'Shea, B. W., Norman, M. L., & Khochfar, S. 2015, *MNRAS*, 452, 2822
- Springel, V. 2005, *MNRAS*, 364, 1105
- Stacy, A., Greif, T. H., & Bromm, V. 2012, *MNRAS*, 422, 290
- Stacy, A., Greif, T. H., & Bromm, V. 2012, *MNRAS*, 422, 290
- Suda, T., Katsuta, Y., Yamada, S., et al. 2008, *PASJ*, 60, 1159
- Suda, T., Hidaka, J., Aoki, W., et al. 2017, *PASJ*, 69, 76
- Susa, H. 2006, *PASJ*, 58, 445
- Susa H., 2013, *ApJ*, 773, 185
- Susa, H., Hasegawa, K., & Tominaga, N. 2014, *ApJ*, 792, 32
- Tominaga, N., Iwamoto, N., & Nomoto, K. 2014, *ApJ*, 785, 98
- Tornatore, L., Ferrara, A., & Schneider, R. 2007, *MNRAS*, 382, 945
- Tornatore, L., Borgani, S., Dolag, K., & Matteucci, F. 2007, *MNRAS*, 382, 1050
- Truelove, J. K., Klein, R. I., McKee, C. F., et al. 1997, *ApJ*, 489, L179
- Umeda, H., & Nomoto, K. 2002, *ApJ*, 565, 385
- Umeda, H., & Nomoto, K. 2003, *Nature*, 422, 871
- Whalen, D., van Veelen, B., O'Shea, B. W., & Norman, M. L. 2008, *ApJ*, 682, 49
- Wise, J. H., Turk, M. J., Norman, M. L., & Abel, T. 2012, *ApJ*, 745, 50
- Xu, H., Wise, J. H., & Norman, M. L. 2013, *ApJ*, 773, 83
- Yoshida, N., Abel, T., Hernquist, L., & Sugiyama, N. 2003, *ApJ*, 592, 645